Radiative transport and collisional transfer of excitation energy in Cs vapors mixed with Ar or He

Cedomil Vadla[a,*], Vlasta Horvatic[a], Kay Niemax[b]

[a]*Institute of Physics, Bijenicka 46, 10000 Zagreb, Croatia*
[b]*Institute of Spectrochemistry and Applied Spectroscopy* (ISAS)*, Bunsen-Kirchhoff-Strasse 11, 44139 Dortmund, Germany*

Abstract

This paper is a review (with a few original additions) on the radiative transport and collisional transfer of energy in laser-excited cesium vapors in the presence of argon or helium. Narrow-band excitation of lines with Lorentz, Doppler and Voigt profiles is studied in order to calculate effective rates for pumping of spectral lines with profiles comprising inhomogeneous broadening components. The radiative transport of excitation energy is considered, and a new, simple and robust, but accurate theoretical method for quantitative treatment of radiation trapping in relatively optically thin media is presented. Furthermore, comprehensive lists of experimental values for the excitation energy transfer cross-sections related to thermal collisions in Cs–Ar and Cs–He mixtures are given. Within the collected cross-section data sets, specific regularities with respect to the energy defect, as well as the temperature, are discerned. A particular emphasis is put on the radiative and collisional processes important for the optimization of resonance–fluorescence imaging atomic filters based on Cs–noble gas systems.
© 2003 Elsevier Science B.V. All rights reserved.

Keywords: Optical excitation; Laser excitation; Energy transfer; Collision transfer; Radiation trapping; Cesium; Alkali–noble gas mixture; Imaging atomic filter

1. Introduction

Theoretical and experimental investigations on radiative transport and collisional excitation energy transfer in gases, vapors and plasmas have a long tradition in physics, since these complex processes have to be fully understood if, for example, astrophysical phenomena are interpreted, plasmas are characterized or discharge lamps for light generation are optimized.

Numerous basic studies have been performed on systems involving alkali vapors and their mixtures with noble gases. There are several reasons why these systems are very suitable subjects for experimental as well as theoretical investigations. Alkali resonance lines are in a spectral range attainable by available lasers and alkali vapors can easily be generated in cells. On the other hand, due to their simple hydrogen-like structure, alkali atoms are convenient subjects for theoretical calculations and for modeling. All these investigations are important contributions to the general basic

*Corresponding author. Fax: +385-1-469-8889.
E-mail address: vadla@ifs.hr (C. Vadla).

understanding of the physical processes in excited atomic systems. They can be found in the literature under keywords such as optical pumping, line broadening, interaction potentials, radiative trapping, diffusion of resonance radiation, collisional excitation energy transfer, etc. On the other hand, there is a large body of work that deals with practical applications of energy exchange processes in mixed vapors or gases. Alkali–noble gas systems used as atomic line filters represent one example.

In an atomic line filter the input radiation at a resonance wavelength is absorbed in an atomic vapor and a radiation output is observed at a different frequency after radiative and non-radiative excitation energy transfer processes. Atomic line filters operate in various metal vapors at numerous discrete wavelengths throughout the UV, visible and near-infrared spectral regions [1,2]. Mixtures of excited Cs or Rb atoms and noble gas atoms have been found to be good candidates for atomic filters. In a passive atomic line filter, no additional optical pumping is applied, while in an active filter the atomic vapor is initially prepared by optical excitation using a laser tuned to the wavelength of an intermediate transition, which enables conversion of the input radiation to the signal at a desired output wavelength. The atomic line filters are ultra-narrow-band filters, which can have various practical applications in applied spectroscopy, for instance in analytical chemistry or in optical communications. Of particular interest are atomic filters operating at the Fraunhofer minima of the solar spectrum, which allow the measurement of weak radiation in the presence of the solar background.

Special classes of the atomic filters are imaging detectors, i.e. two-dimensional atomic line filters. Ultra-narrow-band atomic resonance ionization and fluorescence imaging detectors [1–4] represent a new trend in imaging science with promising practical applications. They are under development for the detection of e.g. moving objects or spatial distributions of excited particles in a medium. Here, besides spectral resolution and quantum efficiency, spatial resolution is the most important characteristic of such detectors. Recently, several investigations [5–10] into cesium-based fluores-

cence imaging filters have been carried out, dealing with the optimization of the basic filter properties to find compromise conditions between optimum efficiency and both spectral and spatial resolution. The experiments were performed with cells filled with pure Cs vapors or mixed with Ar as the buffer gas. Cesium was chosen because of its high vapor density at room temperature and its convenient resonance wavelengths. As pointed out in [9], the laser wavelengths for pumping Cs atoms are in the near-infrared region, which is easily accessible by cw laser diodes. Furthermore, the detectors can be compact, portable and operated with very low power consumption. The experimental findings [5–10] stressed the influence of the pumping schemes chosen and the effects of radiation trapping and collisional mixing on the general efficiency of a Cs imaging filter. It was stated that further investigations of these processes are needed to optimize these systems.

The aim of the present paper is to give specific contributions to the optimization of the Cs imaging filters. In particular, optical pumping, radiation trapping and collisional excitation energy transfer in neutral metal vapors are considered. New aspects as well as new theoretical approximations are presented, which can be useful for the straightforward quantitative analysis of the systems.

The present paper is organized as follows. Section 2 deals with optical pumping i.e. pumping rates and atom number densities created in excited states are considered for narrow-band laser excitation of both homogeneously and inhomogeneously broadened spectral lines. Appropriate relations are obtained, which enable the evaluation of pumping rates and the determination of optimum conditions for optical pumping with respect to maximum excited state number density. In Section 3 approaches are presented that yield a qualitative picture of the radiative transport in atomic vapors leading to trapping and diffusion of resonance radiation. The procedures presented also allow a quantitative treatment of the radiation diffusion and the effective radiation rates at almost optically thin conditions in a simple way. The collisional excitation energy transfer in cesium vapors, pure and mixed with Ar or He, is addressed in Section 4. The elements of experimental and theoretical

approaches to this subject are discussed, and comprehensive lists of experimental cross-section data for various collision excitation energy processes involving cesium atoms taken from literature are given. Taking into account these data, a simple empirical relation between the energy defects and the cross-sections for different excitation energy transfer processes is presented and a general picture of the temperature dependence of the collision cross-section is given. Finally, based on the considerations and theoretical approaches presented, experimental conditions for improvement of the spatial resolution and efficiency of imaging atomic filters are predicted. The relevant spectroscopic and other data concerning cesium are given in Appendices.

2. Optical pumping

Optical pumping can generally be defined as selective population or depletion of energy levels by radiation. There are many aspects of optical pumping, the effects of which depend on the properties of the radiation and the characteristics of the absorbing transition. For instance, if a polarized narrow band light is absorbed in transitions between the states $|1\rangle$ and $|2\rangle$, represented by the electronic angular momenta $\vec{J}_1$ and $\vec{J}_2$ and the corresponding magnetic quantum numbers M_i, then the $2J_i+1$ degenerate substates $|J_i,M_i\rangle$ of the lower and upper level will be unequally depleted and populated. The unequal population, i.e. the polarization of particular Zeeman sublevels, is the consequence of the selection rules for the absorption of the polarized light in the $|1,J_1,M_1\rangle \rightarrow |2,J_2,M_2\rangle$ process and the spontaneous emission in the $|2,J_2,M_2\rangle \rightarrow |1,J_1,M_1\rangle$ process. These optical pumping effects can easily be achieved by classical incoherent light sources and detected by monitoring the anisotropy and polarization of fluorescence light. Long before the invention of the laser, experiments of this type were extensively performed applying spectral lamps, hollow-cathode lamps, radio-frequency discharges, etc. At the same time, the theory of optical pumping was developed. A detailed review on this subject for the period 1924–1971 is given in Ref. [11].

In the following sections, optical pumping by a single mode laser is considered with a view to producing the highest possible population density in an excited atomic state, which is directly related to the efficiency of atomic filters. It is assumed that the atomic vapor is confined in a closed cell at thermal equilibrium and that the absorbing atoms are influenced by atom–atom collisions. Some basic items important for the present considerations is briefly discussed (for more details see Ref. [12]) and the conditions for optimum efficiency of optical pumping of the cesium resonance lines in Cs–noble gas mixtures are discussed.

2.1. Line kernel profiles

In gaseous medium, spectral lines have homogeneous profiles in their kernels due to natural and collision (impact) broadening. The term *homogeneous* is related to the fact that all atoms in the system participate in absorption (or emission) with equal probability. In contrast to that, the lines can also be inhomogeneously broadened due to the Doppler effect [13].

The homogeneously broadened line profile has a Lorentzian shape, given in the normalized form by:

$$P_{\mathrm{L}}(\nu - \nu_{12}) = \frac{1}{2\pi} \frac{\Gamma^\nu}{(\nu - \nu_{12})^2 + (\Gamma^\nu/2)^2} \qquad (2.1)$$

where Γ^ν [s^{-1}] denotes the broadening parameter, which comprises contributions from different homogeneous broadening mechanisms. Note that the broadening parameter is expressed in frequency (emphasized by the superscript ν), not in angular frequency $\omega = 2\pi\nu$. This notation is used throughout the paper. The natural broadening is characterized by the parameter $\Gamma^\nu_{\mathrm{nat}} = A_{21}/2\pi$, where A_{21} is the Einstein coefficient for spontaneous emission. The collision broadening parameters are usually represented in the form $\Gamma^\nu_{\mathrm{col}} = \gamma^\nu_{\mathrm{P}} N_{\mathrm{P}}$, where γ^ν_{P} [s^{-1} m^3] is the broadening rate coefficient and N_{P} [m^{-3}] the perturber number density. Due to natural and collisional broadening, the homogeneous profile is a convolution of individual profiles, which again is a Lorentzian with the broadening parameter $\Gamma^\nu_{\mathrm{tot}} = \Gamma^\nu_{\mathrm{nat}} + \Gamma^\nu_{\mathrm{coll}}$. The peak value of the

Lorentzian profile equals $P_L(0) = 2/(\pi \Gamma_{tot}^\nu)$ and the half-width (full width at half-maximum, FWHM) is $\Delta_L = \Gamma_{tot}^\nu$.

The Maxwellian distribution of atomic velocities in a thermal vapor and the Doppler effect yield a Gaussian line profile, which in the normalized form is represented by:

$$P_G(\nu - \nu_{12}) = \frac{1}{\pi^{1/2} \Delta \nu_D} \exp\left[-\left(\frac{\nu - \nu_{12}}{\Delta \nu_D} \right)^2 \right] \quad (2.2)$$

with $\Delta \nu_D = \nu_{12}(v_m/c)$, where $v_m = (2kT/M_A)^{1/2}$ is the most probable velocity of atoms, while k and M_A are the Boltzmann constant and the mass of the atom, respectively. The peak value of the Gaussian profile is $P_D(0) = 1/(\pi^{1/2} \Delta \nu_D)$ and the full-width at half-maximum amounts to $\Delta_G = 2(\ln 2)^{1/2} \Delta \nu_D$.

When both homogeneous and inhomogeneous broadening processes are present, the full line shape is a convolution of the Lorentzian and the Gaussian profiles. The resulting line shape is known as a Voigt profile, for which an exact analytic expression has not yet been found. There are, however, tabulated data for the normalized Voigt profile $P_V(\nu - \nu_{12}, \alpha)$, where the parameter $\alpha = \Delta_L / \Delta_G$. They can be found e.g. in Ref. [14]. The analysis of these data and fitting to analytical functions yielded approximate analytical expressions for the peak values $P_V(0)$ and the half-widths Δ_V of the normalized Voigt profiles. From the empirical analytic expressions, as given in [15], it follows that the peak value of the normalized Voigt profile can be expressed by the half-widths of the Lorentzian and Gaussian components:

$$P_V(0)$$
$$= \frac{1}{\Delta_V \left[1.065 + 0.447 (\Delta_L / \Delta_V) + 0.058 (\Delta_L / \Delta_V)^2 \right]} \quad (2.3)$$

where the half-width Δ_V of the Voigt profile is given by:

$$\Delta_V = \Delta_L / 2 + \left[(\Delta_L / 2)^2 + \Delta_G^2 \right]^{1/2} \quad (2.4)$$

It should be emphasized that the above relations are accurate to 1% for all values of Δ_L / Δ_D in the range from 0 to ∞.

2.2. Pumping rate as a function of line profiles

For modeling of atomic excitation schemes, a quantitative description of the optical pumping, i.e. knowledge of the pumping rates, is often needed. To establish the relationships between pumping rates and basic characteristics of absorbing transitions, we consider a cell filled with atomic vapor having the total number density N_A at temperature T. The vapor is illuminated by a laser beam with the frequency-dependent spectral intensity $I^\nu(\nu)$ [J m^{-2} s^{-1} Hz^{-1}], which is determined by the power W [J s^{-1}], the bandwidth Δ_{las} [Hz] and the beam cross-section q [m^2]. The laser frequency ν_{las} is tuned to the frequency ν_{12} of the $1 \rightarrow 2$ transition from the ground to an excited state. It is assumed that states 1 and 2 are degenerate and that their Zeeman sublevels are collisionally mixed to such an extent that the polarization effects become negligible. This is valid in experiments with the cesium resonance lines optically pumped by a linearly polarized, single-mode laser beam when, for example, the noble gas pressure is larger than several 10 mbar at room temperature. Information and data for collisional depolarization of Cs resonance lines can be found e.g. in [16]. States 1 and 2 are taken to be well separated mutually and isolated from the other levels, so that all collisional excitation energy transfer processes (see Section 4) can be neglected. In such conditions and taking into account absorption, spontaneous emission and stimulated radiation, the system is described in the steady-state regime by the following simple rate equation for the number densities N_1 and N_2 in the relevant states:

$$\frac{dN_1}{dt} = -\frac{dN_2}{dt} = 0 = -\Pi N_1 + A_{21} N_2 + \frac{g_1}{g_2} \Pi N_2 \quad (2.5)$$

where Π [s^{-1}] is the pumping rate, A_{21} is the Einstein coefficient for spontaneous emission, and g_1 and g_2 label the statistical weight of the lower

and upper state, respectively. The above rate equation is related to an optically thin volume element. Considering the spectral intensity $I^\nu(\nu,x)$ of the beam propagating in the x-direction, the appropriate expression for its change at the position between x and $x+dx$ is:

$$\frac{d}{dx}I^\nu(\nu,x) = -k(\nu)I^\nu(\nu,x) + k'(\nu)I^\nu(\nu,x) \qquad (2.6)$$

where $k(\nu)$ [cm^{-1}] is the linear frequency-dependent absorption coefficient and $k'(\nu)$ is the coefficient for stimulated emission. Here, the contribution by the isotropic spontaneous emission in the x-direction has been neglected. Eq. (2.6) corresponds to Eq. (2.5), and it is obvious that the $k'(\nu)/k(\nu)$ ratio is equal to $(g_1/g_2)(N_2/N_1)$, and that $k'(\nu)$ becomes non-negligible for high intensities of incoming light. In that case, the medium is characterized by a fictitious absorption coefficient $k_S(\nu) = k(\nu)(1-g_1N_2/g_2N_1)$, which is usually called the saturated or non-linear absorption coefficient. However, the actual absorption processes are related to $k(\nu)$, which can be expressed as:

$$k(\nu) = KN_1 P(\nu - \nu_{12}) \qquad (2.7)$$

where K is given by the well-known Ladenburg relation:

$$K = \frac{\pi e^2}{m_e c}f_{12} = \frac{g_2}{g_1}\frac{c^2}{8\pi \nu_{12}^2}A_{21} \qquad (2.8)$$

and $P(\nu - \nu_{12})$ [Hz^{-1}] is the normalized ($\int Pd\nu = 1$) line profile. Here, f_{12} is the line oscillator strength, and e and m_e are the electron charge and mass, respectively. If the line is homogeneously broadened, the first term in Eq. (2.6), integrated over the whole frequency range, yields the total power absorbed per unit volume:

$$Y = KN_1\int P_H(\nu - \nu_{12})I^\nu(\nu)\,d\nu \qquad (2.9)$$

where the subscript H is a reminder of the homogeneous character of the line profile. On the other hand, Y [J s^{-1} m^{-3}] is proportional to the first term in Eq. (2.5):

$$Y = h\nu_{12}\Pi^H N_1 \qquad (2.10)$$

where h is the Planck constant. The combination of Eqs. (2.9) and (2.10) gives an expression for the pumping rate in the case of a homogeneous line profile:

$$\Pi^H = \frac{K}{h\nu_{12}}\int P_H(\nu - \nu_{12})I^\nu(\nu)\,d\nu \qquad (2.11)$$

If we consider the influence of the relationship between the line profile width Δ and the laser bandwidth Δ_{las} on the pump rate, it is useful to make a straightforward analysis in which the line profiles are approximately represented by rectangles. In this model, the square profile $P_{sqr}(\nu - \nu_{12})$, normalized to unit area, is constant and equals $1/\Delta^{sqr}$ for the frequencies in the interval $(\nu_{12} - \Delta^{sqr}/2, \nu_{12} + \Delta^{sqr}/2)$. Outside of this interval it is zero. In the same way, the rectangular laser spectral intensity is $I^\nu_{sqr} = W/q\Delta_{las}$ in the frequency interval $(\nu_{las} - \Delta_{las}/2, \nu_{las} + \Delta_{las}/2)$, and zero otherwise.

In the following, we consider only optical pumping in the center of the line ($\nu_{las} = \nu_{12}$). In the case when

(a) $\Delta_{las} > \Delta^{sqr}$

which corresponds to broadband laser pumping, Eq. (2.11) yields:

$$(\Pi)^a = \frac{KW}{h\nu_{12}q}\frac{1}{\Delta_{las}} \qquad (2.12)$$

which means that the line profile is irrelevant, i.e. the pumping is homogeneously distributed over the whole atomic ensemble. Therefore, Eq. (2.11) can also be used for calculation of the pumping rate of inhomogeneous profiles in the case of broadband pumping. It is plausible that optimal pumping occurs when $\Delta_{las} = \Delta^{sqr}$. Furthermore, in the case when

(b) $\Delta_{las} < \Delta^{sqr}$

the rectangular approximation of a homogeneous profile (width: Δ_H^{sqr}) yields the following expres-

sion for the pumping rate:

$$(\Pi^{\mathrm{H}})^b = \frac{KW}{h\nu_{12}q} \frac{1}{\Delta_{\mathrm{H}}^{\mathrm{sqr}}} \qquad (2.13)$$

Obviously, the pumping rate $(\Pi^{\mathrm{H}})^b$ can be determined without exactly knowing the laser bandwidth. However, the line width of the homogeneous profile is needed.

If the line profile comprises the inhomogeneous component, then N_1 in Eq. (2.9) should be formally replaced by a portion $N_1^{\mathrm{IH}} < N_1$. Since the pumping rate in Eq. (2.10) is defined for the total number density N_1, this implies a lowering of the effective pumping rate. Nevertheless, the integral over the frequencies in Eq. (2.9), which is related to a inhomogeneous absorption coefficient, has no specific physical sense. In this case the determination of the pumping rate is not simple and this issue is treated in the following subsection.

2.3. Single-mode laser excitation in the line kernel

For practical and economic reasons, diode lasers are the only true candidates for realization of active atomic filters and imaging detectors. They can be multimode (power of the order of magnitude of 1 W) or single mode (typical power up to 100 mW). However, the modes of a multimode diode laser are typically 0.2 nm apart, which greatly exceeds the Doppler widths at temperatures somewhat above room temperature. Therefore, typical pumping in the kernel of the spectral line with a stabilized multimode laser is equivalent to single-mode laser pumping.

In the following, we consider single-mode pumping of a spectral line having a profile comprising the homogeneous and inhomogeneous broadening contributions. Here, we assume that the laser width Δ_{las} (typical value approx. 10 MHz) is very small in comparison with the widths of both homogeneous and inhomogeneous profile components ($\Delta_{\mathrm{las}} \ll \Delta_{\mathrm{L}}, \Delta_{\mathrm{G}}$). Therefore, in the following, the laser line profile is represented by the δ-function, i.e. the laser spectral intensity is described by $I^\nu(\nu) = (W/q) \cdot \delta(\nu - \nu_{\mathrm{las}})$.

2.3.1. Pure Lorentzian profile

In the case of a pure Lorentzian profile ($\Delta_{\mathrm{L}} \gg \Delta_{\mathrm{G}}$) and for the laser detuning $\Delta\nu_{\mathrm{las}} = \nu_{\mathrm{las}} - \nu_{12}$, the detuning-dependent pumping rate Π^{L}, obtained via Eqs. (2.1) and (2.11), reads as follows:

$$\Pi^{\mathrm{L}}(\Delta\nu_{\mathrm{las}}) = \frac{1}{2\pi} \frac{KW}{h\nu_{12}q} \frac{\Delta_{\mathrm{L}}}{(\Delta\nu_{\mathrm{las}})^2 + (\Delta_{\mathrm{L}}/2)^2} \qquad (2.14)$$

For the sake of clarity in the following text, here we define the pumping rate Π^{LC} for the center of the Lorentzian profile ($\Delta\nu_{\mathrm{las}} = 0$):

$$\Pi^{\mathrm{LC}} = \frac{2}{\pi} \frac{KW}{h\nu_{12}q} \frac{1}{\Delta_{\mathrm{L}}} \qquad (2.15)$$

and the rate Π^{LW} for the pumping in the Lorentzian wing ($\Delta\nu_{\mathrm{las}} \gg \Delta_{\mathrm{L}}$):

$$\Pi^{\mathrm{LW}}(\Delta\nu_{\mathrm{las}}) = \frac{1}{2\pi} \frac{KW}{h\nu_{12}q} \frac{\Delta_{\mathrm{L}}}{(\Delta\nu_{\mathrm{las}})^2} \qquad (2.16)$$

Since for the homogeneous line broadening the absorption is equally probable for each atom in the vapor, the detuning–dependent ratio N_2/N_{A}, obtained by combination of Eqs. (2.5) and (2.14), is $N_2/N_{\mathrm{A}} = (\Pi^{\mathrm{L}}/A_{21})/[1 + (\Pi^{\mathrm{L}}/A_{21})(1 + g_1/g_2)]$. In turn, the pumping rate Π^{L} can be formally expressed in terms of the established population ratio N_2/N_{A} as follows:

$$\Pi^{\mathrm{L}}(\Delta\nu_{\mathrm{las}}) = A_{21} \frac{\dfrac{N_2(\Delta\nu_{\mathrm{las}})}{N_{\mathrm{A}}}}{1 - (1 + g_1/g_2)\dfrac{N_2(\Delta\nu_{\mathrm{las}})}{N_{\mathrm{A}}}} \qquad (2.17)$$

The form of Eq. (2.17) is used in the next subsection for the determination of effective pumping rates in cases of inhomogeneous line broadening.

2.3.2. Nearly pure Doppler profile

In thermal equilibrium, the number density $dN_{\mathrm{A}}(v_{\mathrm{x}})$ of the atoms with a velocity component between v_{x} and $v_{\mathrm{x}} + dv_{\mathrm{x}}$ is given by the Maxwellian

distribution:

$$dN_A(v_x) = \frac{N_A}{\sqrt{\pi}\,v_m} \exp\left[-\left(\frac{v_x}{v_m}\right)^2\right]\,dv_x \qquad (2.18)$$

Due to the Doppler effect, for the laser detuning $\Delta v_{las} = v_{las} - v_{12}$ only atoms with the velocity component $v_x = (c/v_{12})\Delta v_{las}$ can absorb photons of frequency v_{las} propagating in the x-direction. However, due to homogeneous line broadening, a correspondingly larger portion of atoms can participate in absorption.

First, we present a semi-quantitative approach using the rectangular approximation for the shape of the homogeneous line profile, since it is quite illustrative for the subject considered. In this approximation, the number density N_A^{IH} of atoms able to absorb incoming photons is determined by v_x being in the interval between v_x^- and v_x^+, where:

$$v_x^{\pm} = (c/v_{12})(\Delta v_{las} \pm \Delta_H^{sqr}) \qquad (2.19)$$

In the simple two-level approach, with the selected velocity group of atoms taken as conserved during the absorption and emission of a photon, the following relationship is valid:

$$N_A^{IH} = N_1^{IH} + N_2^{IH} \qquad (2.20)$$

For $v_x^{\pm}$ sm<u>all</u> compared with v_m, i.e. when $\Delta_H^{sqr} \ll \Delta_G = 2\sqrt{\ln 2}\,v_{12}(v_m/c)$, the detuning-dependent number density N_A^{IH}, labeled with N_A^{nD} in the case at hand, is given by:

$$N_A^{nD}(\Delta v_{las}) \approx \frac{N_A}{\sqrt{\pi}\,v_m} e^{-4\ln 2(\Delta v_{las}/\Delta_G)^2} \int_{v_x^-}^{v_x^+} dv_x$$

$$= 4\sqrt{\frac{\ln 2}{\pi}} e^{-4\ln 2(\Delta v_{las}/\Delta_G)^2} \frac{\Delta_H^{sqr}}{\Delta_G} N_A, \quad \Delta_H^{sqr} \ll \Delta_G \qquad (2.21)$$

Taking into account Eq. (2.20), the rate equation for the number densities N_1^{nD} and N_2^{nD}, written analogously to Eq. (2.5), yields the following expression for the number density N_2^{nD} of the excited atoms:

$$N_2^{nD}(\Delta v_{las})$$
$$= \frac{\Pi^H/A_{21}}{1 + (\Pi^H/A_{21})(1 + g_1/g_2)} N_A^{nD}(\Delta v_{las}),$$
$$\Delta_H^{sqr} \ll \Delta_G \qquad (2.22)$$

where the pumping rate Π^H is given by Eq. (2.13). In the case when the saturation parameter $\Pi^H/A_{21} \gg 1$, the considered velocity group of atoms is strongly saturated, but the number density of the atoms in the excited state is small compared with the total number density N_A. This is the case of strong burning of Bennet holes in the velocity distribution [12].

By analogy with Eq. (2.17), the effective rate Π_{eff}^{nD} related to all atoms can, in terms of ratios N_2^{nD}/N_A, be defined as:

$$\Pi_{eff}^{nD}(\Delta v_{las}) = A_{21} \frac{\dfrac{N_2^{nD}(\Delta v_{las})}{N_A}}{1 - (1 + g_1/g_2)\dfrac{N_2^{nD}(\Delta v_{las})}{N_A}}$$

$$\approx A_{21} \frac{N_2^{nD}(\Delta v_{las})}{N_A}, \quad \Delta_H^{sqr} \ll \Delta_G \qquad (2.23)$$

For example, in the case of strong pumping ($\Pi^H/A_{21} \gg 1$) the combination of Eqs. (2.23), (2.22) and (2.21) yields for pumping in the line center:

$$\frac{\Pi_{eff}^{nD}(0)}{A_{21}} \approx \frac{4\sqrt{\ln 2/\pi}}{1 + g_1/g_2} \frac{\Delta_H^{sqr}}{\Delta_G},$$
$$\Delta_H^{sqr} \ll \Delta_G, \ \Pi^H/A_{21} \gg 1 \qquad (2.24)$$

which is obviously much smaller than 1. In the limit $\Pi^H/A_{21} \ll 1$, the effective pumping rate is related to Π^H as follows:

$$\Pi_{eff}^{nD}(0) \approx 4\sqrt{\ln 2/\pi} \frac{\Delta_H^{sqr}}{\Delta_G} \Pi^H,$$
$$\Delta_H^{sqr} \ll \Delta_G, \ \Pi^H/A_{21} \ll 1 \qquad (2.25)$$

However, from the efficiency standpoint of an

atomic filter, it is important to obtain the highest possible excited-state number density. In the case of single-mode pumping, that can be simply and efficiently realized by increasing the homogeneous half-width [see Eq. (2.24)], for instance by increasing the buffer gas pressure.

2.3.3. Combination of Doppler and Lorentzian profiles

In the following step we consider single-mode pumping of a spectral line with Lorentzian shape of the homogeneous profile component. For the Lorentz profile and for the given laser detuning, the corresponding portion N_A^{IH}, labeled as N_A^{DL}, is determined by a convolution of velocity component distribution [Eq. (2.18)] and the profile $P_L' = (\pi\Delta_L/2)P_L(\Delta\nu_{las} - v_x(\nu_{12}/c))$, where the variable of integration is v_x. In contrast to P_L [see Eq. (2.1)], the Doppler-shifted Lorentzian P_L' is dimensionless and is normalized to unity in the line center. Note that Eq. (2.21) can be formally regarded as a convolution of the velocity distribution and the homogeneous square profile, where the latter is normalized to have height equal to 1.

The convolution yields detuning–dependent N_A^{DL}, which may be represented in the form:

$$N_A^{DL}(u,\alpha) = f_V(u,\alpha)N_A \quad (2.26)$$

where the relative detuning u is defined as:

$$u = (\nu_{las} - \nu_{12})/\Delta_G \quad (2.27)$$

and the broadening parameter α, as already defined in Section 2.1, is:

$$\alpha = \Delta_L/\Delta_G \quad (2.28)$$

The Voigt function $f_V(u,\alpha)$, the value of which is in the interval between 0 and 1 for all values of u and α, is given by:

$$f_V(u,\alpha) = \frac{1}{4\sqrt{\pi}} \int_{-\infty}^{+\infty} \exp(-\varsigma^2)$$
$$\times \frac{\alpha^2}{\left(u - \varsigma/2\sqrt{\ln 2}\right)^2 + \left(\alpha/2\right)^2} \, d\varsigma \quad (2.29)$$

where the variable of integration is $\zeta = v_x/v_m$.

The rate equation for the number densities N_1^{DL} and N_2^{DL} with appropriate pumping rate Π^{LC} [see Eq. (2.15)] yields the following expression for the detuning-dependent number density N_2^{DL}:

$$N_2^{DL}(u,\alpha,\beta) = f_V(u,\alpha)\frac{\dfrac{\beta}{\alpha}}{1 + \dfrac{\beta}{\alpha}(1 + g_1/g_2)}N_A \quad (2.30)$$

where the pumping parameter β is defined by:

$$\beta = \frac{2KW}{\pi h\nu_{12}qA_{21}}\frac{1}{\Delta_G} \quad (2.31)$$

The calculated dependence of $N_2^{DL}(0,\alpha,\beta)/N_A$ on parameters α and β for single-mode pumping in the line center is shown in Fig. 1a. The calculations were performed for the case when $g_1 = g_2$. As can be observed in Fig. 1a, an optimum population density in the excited state for moderate pumping power (parameter $\beta \leq 3$) appears when $\alpha \approx 1$. A further increase in pumping power does not produce a significant rise in the population of the excited state.

For instance, in the case of the Cs D_2 resonance line at 300 K, the Doppler width of a particular hyperfine component is $\Delta_G = 380$ MHz. Using the cesium vapor pressure curve given in Appendix C and the value for the broadening parameter γ_{Cs}^ν given in Appendix D, we obtain a Lorentzian half-width that is approximately two orders of magnitude smaller than Δ_G. However, adding approximately 50-mbar argon gas with $\gamma_{Ar}^\nu = 2.5 \times 10^{-10}$ s^{-1} (see Appendix D) makes the Lorentzian width comparable with the Doppler width, i.e. creates optimum pumping efficiency. At this point it should be stressed that, under the physical conditions defined here, the decrease in noble gas pressure below several 10 mbar, besides lowering the pumping efficiency, also removes the effects of collisional depolarization of the Zeeman substates. In the limit of pure cesium equilibrium vapors near room temperature, we should take into account strong polarization effects appearing when the Cs first resonance states are excited by polarized narrow-band light [11,16].
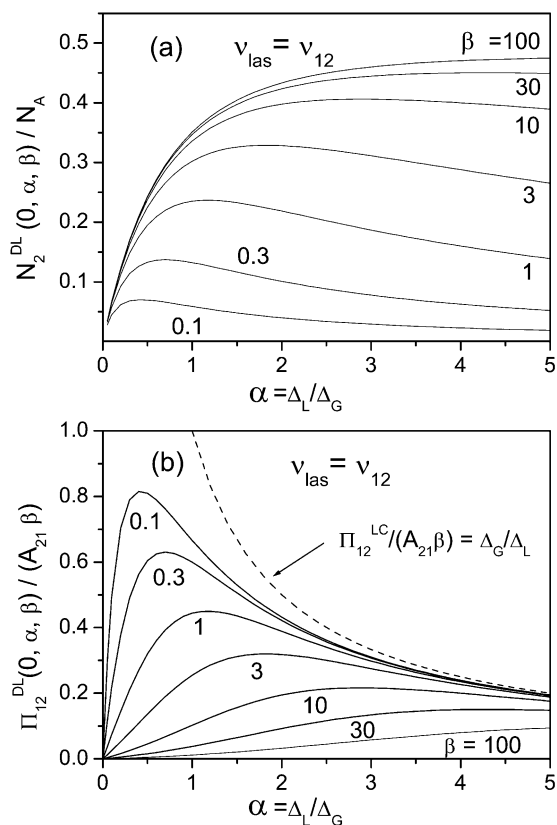
Fig. 1. (a) The calculated excited/total atom number density ratio $N_2^{DL}(\Delta\nu_{las}=0,\alpha,\beta)/N_A$ as a function of the ratio of the Lorentzian and Gaussian line widths $\alpha=\Delta_L/\Delta_G$ for a series of pumping parameters β, in the case of single-mode pumping in the center of the line comprising inhomogeneous and homogeneous broadening. (b) The relative effective pumping rate $\Pi_{eff}^{DL}(0,\alpha,\beta)/A_{21}\beta$ for single-mode pumping in the center of the line comprising inhomogeneous and homogeneous broadening, as a function of the $\alpha=\Delta_L/\Delta_G$ ratio and pumping parameter β. The dashed line indicates the relative rate for pumping homogeneously broadened (Lorentzian) line.

The effective pumping rates $\Pi_{eff}^{DL}(u,\alpha,\beta)$ were calculated by analogy with Eqs. (2.17) and (2.23) from the field of $N_2^{DL}(u,\alpha,\beta)/N_A$ curves via:

$$\Pi_{eff}^{DL}(u,\alpha,\beta)=A_{21}\frac{\dfrac{N_2^{DL}(u,\alpha,\beta)}{N_A}}{1-2\dfrac{N_2^{DL}(u,\alpha,\beta)}{N_A}}, \quad g_1=g_2$$

(2.32)

The results obtained for the pumping in the line center, expressed as the ratio $\Pi_{eff}^{DL}(0,\alpha,\beta)/A_{21}\beta$, which we call the relative effective pumping rate, are plotted vs. Δ_L/Δ_G in Fig. 1b. In the present notation, the Lorentzian pumping rate [Eq. (2.14)] is described by:

$$\Pi^L(u,\alpha,\beta)=A_{21}\beta\frac{\alpha}{4u^2+\alpha^2}$$

(2.33)

For comparison, the hyperbolic curve $\Pi^{LC}/A_{21}\beta=\Delta_G/\Delta_L$ is also plotted in Fig. 1b. As can be observed, when a line having the Voigt profile is pumped by a narrow-band laser, the effective pumping rate strongly depends on the parameter β, i.e. on the applied laser power density. However, in the limit $\beta\ll1$ and for $\alpha\geq1$, the effective pumping rate Π_{eff}^{DL} approaches the values of Π^L. The present representation is very convenient for establishing the relationships between effective pumping rates and the rates corresponding to the homogeneous component of the line profile considered. For instance, in the case of line-center pumping and for $\alpha=1$, the following relationship is obtained by fitting the data displayed in Fig. 1b:

$$\Pi_{eff}^{DL}(0,1,\beta)=\frac{1}{1.42+0.83\beta}\Pi^L(0,1,\beta), \quad g_1=g_2$$

(2.34)

The numerical accuracy of the latter expression is better than 0.01% for β values between 0 and 100. If $\beta\rightarrow\infty$ (case of strong pumping), then Eq. (2.34) yields $\Pi_{eff}^{DL}(0,1,\infty)=A_{21}/0.83$, which means that the maximum saturation parameter is $\Pi_{eff}^{DL}/A_{21}=1.2$.

2.4. Pumping in the Lorentzian wing of the Voigt profile

In order to reach very high populations in the excited state, it is obvious that N_A, i.e. the temperature T of the metal vapor cell, should be increased as much as possible. However, for the given power and bandwidth of the laser, a finite saturation parameter and consequently a finite
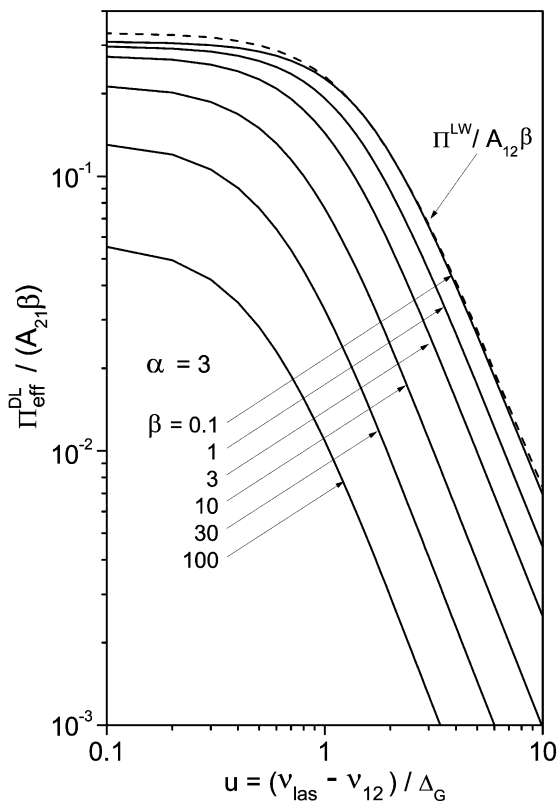
Fig. 2. The effective rate $\Pi_{\text{eff}}^{\text{DL}}(u,\alpha,\beta)$ for pumping the line comprising inhomogeneous and homogeneous broadening as a function of laser detuning $u=(\nu_{\text{las}}-\nu_{12})/\Delta_{\text{G}}$ for a series of pumping parameters β in the case of $\alpha=3$. The dashed line indicates the relative rate for pumping homogeneously broadened (Lorentzian) line in the line wing ($u\gg\alpha$).

absorption coefficient occurs. Thus, attenuation of the laser beam takes place in accordance with the Lambert–Beer exponential law, and this produces a spatially inhomogeneous number density N_2 in the excited state. Nevertheless, under the conditions of an optically thick line center, uniform and efficient pumping in the whole vapor volume can be achieved by laser excitation in the optically thin line wing.

We have calculated the detuning-dependent effective pumping rates $\Pi_{\text{eff}}^{\text{DL}}(u,\alpha,\beta)$ using Eqs. (2.30) and (2.32) for a series of α and β parameters in the range $1\leq\alpha\leq100$ and $0.1\leq\beta\leq100$. For illustration, the results for $\alpha=3$ are shown in Fig. 2. As can be observed, the effective pumping

rate acquires the form of the Lorentzian wing ($\sim u^{-2}$) for a relative detuning several-fold (~ 5) greater than α. To obtain a relationship between Π^{LW} and the effective rate $\Pi_{\text{eff}}^{\text{DLW}}$ for the pumping in the Lorentzian wing of the Voigt profile, we have calculated the ratios $\Pi_{\text{eff}}^{\text{DLW}}(u\geq 5\alpha,\alpha,\beta)/\Pi^{\text{LW}}(u\geq 5\alpha,\alpha,\beta)$. The results as a function of α and β are depicted in Fig. 3. Analysis of the results displayed has shown that the relation:

$$\Pi_{\text{eff}}^{\text{DLW}}(u\geq 5\alpha,\alpha,\beta)$$
$$= \frac{1}{1+2(\beta/\alpha)}\Pi^{\text{LW}}(u\geq 5\alpha,\alpha,\beta),$$
$$g_1=g_2,\ \alpha\geq 1 \tag{2.35}$$

holds with the numerical accuracy better than $1:10^5$ for the α and β parameters in the range stated above. Substitution of Eqs. (2.33), (2.31), (2.28) and (2.27) into Eq. (2.35) yields a more detailed expression for $\Pi_{\text{eff}}^{\text{DLW}}$:

$$\Pi_{\text{eff}}^{\text{DLW}}(\Delta\nu_{\text{las}})$$
$$= \frac{1}{1+\dfrac{4KW}{\pi h\nu_{12}q}\dfrac{1}{A_{21}\Delta_{\text{L}}}}\frac{KW}{2\pi h\nu_{12}q}\frac{\Delta_{\text{L}}}{(\Delta\nu_{\text{las}})^2},$$
$$\Delta\nu_{\text{las}}\geq 5\Delta_{\text{L}},\ \Delta_{\text{L}}\geq\Delta_{\text{G}} \tag{2.36}$$
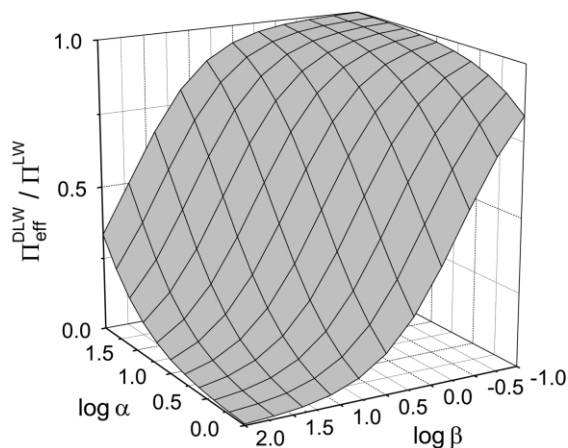

Fig. 3. The ratio of the effective rate for pumping the Voigt profile in the Lorentzian wing and the rate for pumping pure Lorentzian profile in the line wing $\Pi_{\text{eff}}^{\text{DLW}}/\Pi^{\text{LW}}$ calculated for detunings $u\geq 5\alpha$ and displayed as a function of α and β for parameter values in the range $1\leq\alpha\leq100$ and $0.1\leq\beta\leq100$.

In the limit of strong pumping $(W \to \infty)$, $\Pi_{\mathrm{eff}}^{\mathrm{DLW}} = 0.125 A_{21} (\Delta_{\mathrm{L}} / \Delta \nu_{\mathrm{las}})^2$.

Obviously, this rate is smaller than the rate obtained by pumping in the line center. However, at higher N_{A}, trapping effects start to play a significant role. Radiation trapping refers to the fact that the absorbed, and subsequently spontaneously emitted, photons can be absorbed and re-emitted several times before finally reaching the cell window. A comprehensive overview dealing with the problem of trapping is given in Ref. [17]. As a consequence of this multiple re-absorption and re-emission, the effective lifetime in the excited state, related to photon escape from the whole excited volume, is prolonged, i.e. the effective radiative rate A_{21}^{eff} is smaller than the Einstein coefficient A_{21} (see Section 3). The simple rate equation [Eq. (2.5)], related to an optically thin volume element, cannot be applied for the description of such systems, since trapping is a volume effect. Nevertheless, in the case of weak pumping in the Lorentzian wing $(N_2 / N_{\mathrm{A}} \ll 1)$, stimulated emission can be neglected and the balance in the whole volume considered yields:

$$\bar{N}_2 = \frac{\Pi_{\mathrm{eff}}^{\mathrm{DLW}}}{A_{21}^{\mathrm{eff}}} N_{\mathrm{A}} \qquad (2.37)$$

where $\bar{N}_2$ is the spatial average of N_2. The values for A_{21}^{eff} are usually estimated using the results obtained by Holstein [18,19], who studied in detail two volume shapes: an infinitely long cylinder and an infinite slab. In both cases, the limit of strong absorption in the line kernel has been considered for two extremes: a pure Doppler and pure Lorentzian line profile. In the case of an infinitely long cylinder with the radius R_{C} (a similar situation as for a long absorption cell) and in the case of a pure Lorentzian profile, the Holstein approximation yields:

$$A_{21}^{\mathrm{eff}} = \frac{1.115}{(\pi k_0^{\mathrm{L}} R_{\mathrm{C}})^{1/2}} A_{21} \qquad (2.38)$$

where k_0^{L} is the peak value of the absorption coefficient, i.e. $k_0^{\mathrm{L}} = 2 K N_{\mathrm{A}} / \pi \Delta_{\mathrm{L}}$. It should be emphasized that Eq. (2.38) is valid for the optical

depths $k_0^{\mathrm{L}} R_{\mathrm{C}}$ being approximately in the range between 5 and 100. At optical depths higher than 100, A_{eff} becomes nearly constant over a wide range of large optical depths (see for example the case of sodium in Ref. [20]).

In the case of the cesium D_1 and D_2 lines at $N_{\mathrm{Cs}} \geq 10^{13}$ cm^{-3} (and a cell radius of approx. 1 cm) the effective rates are approximately two orders of magnitude smaller than the radiative rate A_{21} (see Appendix E). An increase in the ground-state number density N_{A} has the favorable effect so that not only is there an increase in the population of the excited state by pumping, but also by lowering of the effective spontaneous emission rate [see Eq. (2.37)].

Although pumping in the optically thin line wing produces a rate that is smaller than that realized by pumping in the line center [compare Eqs. (2.34) and (2.36)], due to radiative trapping, a significant and spatially uniform population in the excited state can be produced, which is on the track of achieving high quantum efficiency of atomic filters.

3. Radiation trapping

As stated previously, a detailed treatment of the radiation trapping can be found in [17], which also comprises a list of nearly 1000 most relevant works published up to 1996. This book [17] yields insights into the physical mechanisms of radiation trapping and can serve as a toolbox of mathematical methods to solve various radiation trapping problems in practice. In addition, historical progress of investigations in this field has been overviewed, showing that, at particular stages in the development of this field, several times independent groups of atomic physicists and astrophysicists made equivalent contributions at the same or slightly different times.

Trapping problems are usually analyzed in media characterized by high opacity at the relevant spectral lines. Due to trapping, the lifetimes of the resonance states can be prolonged by up to three orders of magnitude, which makes the resonance states act as quasi-metastable states.

As for the atomic line filters, they can be regarded as textbook examples of practical situa-

tions in which trapping plays a vital role. Discussion on the positive influence of strong trapping on the quantum efficiency of an atomic line filter can be found in Ref. [17]. Nevertheless, regarding the spatial resolution of an atomic imaging filter, trapping is an especially undesired effect. For example, when only part of a volume with metal vapor is excited in such imaging detectors [8], the subsequent re-absorption and re-emission processes produce excited atoms far outside of the original excitation zone. This diffusion-like effect can strongly degrade the spatial resolution of the imaging atomic line filter.

Since imaging atomic line filters should have as high quality as possible, it is obvious that the region of relatively small optical depths, where trapping effects start to play an important role, is of particular interest. For this reason, we consider here radiation trapping for optical depths lower than 1 in a way that can be useful for finding experimental conditions for optimum spatial resolution of atomic imaging filters.

3.1. Rate equation approach

Following the considerations in the previous section, the problem of trapping can easily be defined in terms of additional optical pumping rates appearing in dense, excited media. For this purpose, we consider again the cell filled with atomic vapor illuminated by a light beam matching the $1 \rightarrow 2$ transition. Here, we assume low intensity of the incoming light and neglect stimulated emission. Furthermore, we assume significant opacity of the medium at the frequency of the transition considered. The latter assumption means that the spontaneously emitted photons can be absorbed and re-emitted in the media again. Then, the appropriate equation for the power balance in a selected optically thin volume element ΔV_n at position $\vec{r}_n$ within the volume V illuminated by the laser beam (see Fig. 4a) is:

$$\Pi(\vec{r}_n)N_1(\vec{r}_n)\Delta V_n h\nu_{12}$$
$$-A_{21}N_2(\vec{r}_n)\Delta V_n h\nu_{12}+X_n=0 \qquad (3.1)$$
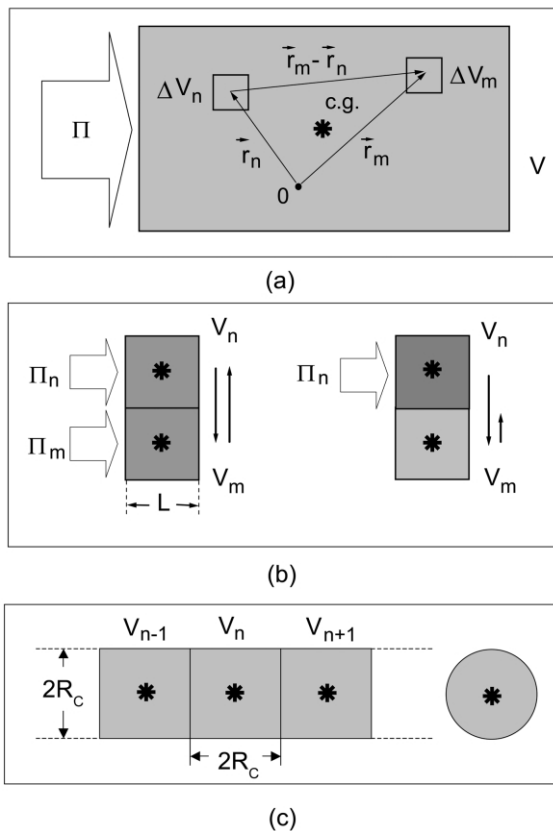

(a)

(b)

(c)

Fig. 4. Schematic illustration of the trapping and resonance radiation diffusion processes. For detailed explanations see the text in Section 3.

where $\Pi(\vec{r}_n)$ is the position-dependent pumping rate for the $1 \rightarrow 2$ transition. In contrast to Eq. (2.5), we have here not only the position-dependent number densities, but also the additional 'pumping' term X_n, which represents absorption in ΔV_n of the spontaneously emitted radiation from the rest of the excited volume:

$$X_n = \sum_{m \neq n} X_{mn} \qquad (3.2)$$

where, X_{nm} [J s^{-1}] is the power of the radiation from volume element ΔV_m that is reabsorbed in the volume ΔV_n. The power W_m [J s^{-1}] emitted from volume ΔV_m is given by:

$$W_m = A_{21} N_2\left(\vec{r}_m\right) \Delta V_m h \nu_{12} \qquad (3.3)$$

At this point, it is crucial to define the spatial and spectral distribution of re-emitted light from a selected volume element. We assume that the spontaneous emission is isotropic and, in addition, that all atoms emit the same, fully spectrally-redistributed spectrum, which is the same as the absorption profile $P(\nu)$. It should be noted that the same assumption was made by Holstein [18]. Now, the spectral intensity $I_{mn}^{\nu}(\nu)$ [J m^{-2} s^{-1} Hz^{-1}] at position $\vec{r}_n$, which is spontaneously emitted in the volume ΔV_m and exponentially attenuated along the path $\left|\vec{r}_m - \vec{r}_n\right|$, can be expressed as:

$$I_{mn}^{\nu}(\nu) = \frac{W_m}{4\pi\left|\vec{r}_m - \vec{r}_n\right|^2} P(\nu)\exp\left[-k(\nu)\left|\vec{r}_m - \vec{r}_n\right|\right]$$
$$(3.4)$$

The volume ΔV_n is characterized by an absorption coefficient $k(\nu)$ at the transition $1 \to 2$. The absorbed power per unit volume X_{mn} is defined analogously to Eq. (2.9):

$$X_{mn} = \Delta V_n \int k(\nu) I_{mn}^{\nu}(\nu) \; \mathrm{d}\nu \qquad (3.5)$$

By substituting Eqs. (3.5), (3.4), (3.3) and (3.2) into Eq. (3.1), we obtain the following relation for the number densities at position $\vec{r}_n$:

$$A_{21} N_2\left(\vec{r}_n\right) - A_{21} \sum_{m \neq n} \Delta V_m N_2\left(\vec{r}_m\right) F\left(\left|\vec{r}_m - \vec{r}_n\right|\right)$$
$$= \Pi\left(\vec{r}_n\right) N_1\left(\vec{r}_n\right) \qquad (3.6)$$

where the function $F\left(\left|\vec{r}_m - \vec{r}_n\right|\right)$ is given by:

$$F\left(\left|\vec{r}_m - \vec{r}_n\right|\right) = \frac{\int_{\nu} k(\nu) P(\nu)\exp\left[-k(\nu)\left|\vec{r}_m - \vec{r}_n\right|\right] \; \mathrm{d}\nu}{4\pi\left|\vec{r}_m - \vec{r}_n\right|^2}$$
$$(3.7)$$

By replacing the sum in Eq. (3.6) by a volume integral where $\vec{r}_m$ and $\vec{r}_n$ become $\vec{r}'$ and $\vec{r}$, respectively, we obtain the steady-state equation of Holstein [18] with an external source $\Pi\left(\vec{r}\right)N_1\left(\vec{r}\right)$:

$$A_{21} N_2\left(\vec{r}\right) - A_{21} \int_{\mathrm{vol}} N_2\left(\vec{r}'\right)$$
$$\times F\left(\left|\vec{r}' - \vec{r}\right|\right) \; \mathrm{d}^3\vec{r}' = \Pi\left(\vec{r}\right)N_1\left(\vec{r}\right) \qquad (3.8)$$

The above equation, with no source part, was derived by Holstein [18] and in the literature it is known as the Holstein or Holstein–Biberman equation [17,20].

The Holstein integral Eq. (3.8) is the equation for the spatially dependent number densities of the atoms in the excited state. A general solution of the Holstein equation does not exist. For every particular case, with given boundary conditions, the solution can be obtained only by making suitable approximations. In the Holstein approximation [19], the solutions were obtained for $k(\nu)$ $\times\left|\vec{r}_m - \vec{r}_n\right| \gg 1$ for a geometry reduced to a quasi one-dimensional case. For instance, in the case of an infinite slab the number densities of atoms in the excited state are taken to be independent of two space coordinates. In addition, as mentioned in Section 2, the Holstein approximation is related to pure Doppler and pure Lorentzian profiles. Because of their convenient explicit form, the results of the Holstein approximation became widely used in spectroscopy for situations in which media exhibited a strong trapping effect. In contrast, in the next subsection we consider the trapping effect for a finite volume and low optical depths.

3.2. Low opacity and constant number-density approximation

We consider a finite volume of the size Λ^3. The atoms are excited by spatially uniform optical pumping at the transition $1 \to 2$, i.e. we assume the pumping rate Π to be independent of the space coordinates. At uniform pumping $[\Pi\left(\vec{r}\right) = \Pi = $ constant], the number densities $N_1\left(\vec{r}\right)$ and $N_2\left(\vec{r}\right)$

can be regarded as weakly dependent on spatial co-ordinates and, in a straightforward approach, the position-dependent number densities can be replaced by average values $\bar{N}_1$ and $\bar{N}_2$, respectively. This implies that the integral in Eq. (3.8) should be related to the average value of $\vec{r}$ in the volume considered, i.e. to the center of gravity where the contributions from the rest of the volume are the largest. Therefore, we take $\vec{r} \equiv \vec{r}_{cg}$, where $\vec{r}_{cg}$ is the position of the center of gravity (see Fig. 4a).

Hence, the integral Eq. (3.8) reduces to the linear equation:

$$A_{21}\bar{N}_2 - A_{21}\bar{N}_2 \int_{vol} F\left(\left|\vec{r}' - \vec{r}_{cg}\right|\right) \, d^3\vec{r}' = \Pi \bar{N}_1 \quad (3.9)$$

If we look for the simplest way to reduce the problem described by Eq. (3.9), it is apparent that the volume integral is most easily solved by assuming spherical symmetry. Although this geometry is of no particular interest regarding further considerations in the present paper, it is, nevertheless, very convenient for transparent demonstration of the validity of the approximations that are made. With the substitution $\rho = \left|\vec{r}' - \vec{r}_{cg}\right|$, the volume integral in Eq. (3.9) in spherical coordinates reduces to:

$$J_{sph} = \int_{sph} F\left(\left|\vec{r}' - \vec{r}_{cg}\right|\right) \, d^3\vec{r}'$$
$$= \int_0^{R_S} \left[\int_\nu k(\nu)P(\nu)\exp\left[-k(\nu)\rho\right] \, d\nu\right] \, d\rho \quad (3.10)$$

where R_S is the radius of the spherical volume considered. In accordance with the initial assumption of low opacity, the exponential function in Eq. (3.10) can be represented by the first three terms of the Taylor series:

$$\exp\left[-k(\nu)\rho\right] \approx 1 - k(\nu)\rho + \frac{1}{2}(k(\nu)\rho)^2 \quad (3.11)$$

which is a good approximation for $k(\nu)\rho < 0.5$.

Table 1
Numerical values of the coefficients $a_i^P = (P(0))^{-i} \int_\nu (P(\nu))^{i+1} d\nu$ for the Doppler and Lorentzian profile

i	a_i^D	a_i^L
1	0.707	0.500
2	0.577	0.375
3	0.500	0.312
4	0.447	0.273
5	0.408	0.246
6	0.377	0.225
7	0.353	0.209
8	0.333	0.196
9	0.316	0.185
10	0.301	0.176

With this approximation, we obtain the following result for the integral J_{sph}:

$$J_{sph} \approx a_1^P(k_0^P R_S) - \frac{a_2^P}{2}(k_0^P R_S)^2 + \frac{a_3^P}{2 \cdot 3}(k_0^P R_S)^3 \quad (3.12)$$

where $k_0^P = K\bar{N}_1 P(0)$ is the peak absorption coefficient, while the dimensionless coefficients a_i^P are of the following form:

$$a_i^P = \frac{1}{(P(0))^i} \int_\nu (P(\nu))^{i+1} \, d\nu \quad (3.13)$$

For pure Lorentzian and pure Doppler profiles, the corresponding coefficients a_1^L and a_1^D are $1/2$ and $1/\sqrt{2}$, respectively. The calculations (see Table 1) show that these coefficients are always smaller than 1 and, in addition, they decrease slowly when i increases. For $k_0^P R_S \leq 0.4$, the first term in Eq. (3.12) is dominant. Even when $k_0^P R_S = 0.4$, its contribution to J_{sph} amounts to approximately 95%. Therefore, in the present approximation it is justified to take $J_{sph} \approx a_1^P k_0^P R_S$ for $k_0^P R_S \leq 0.4$.

In view of the further consideration presented, cube- or cylinder-shaped volumes are of interest. In the case of a cylinder with radius R_C and height $2R_C$, the corresponding integral J_{cyl} is given by:

$$J_{cyl} \approx 1.13 a_1^P k_0^P R_C, \quad k_0^P R_C \leq 0.35 \quad (3.14)$$

In the case of a cube with volume L^3, the calculation yields:

$$J_{\text{cub}} \approx 0.64 a_1^{\text{P}} k_0^{\text{P}} L, \quad k_0^{\text{P}} L \leq 0.6 \tag{3.15}$$

For the particular geometry and corresponding J, Eq. (3.9) yields a number density in the excited state:

$$\bar{N}_2 = \frac{\Pi}{A_{21}(1-J)} \bar{N}_1 \tag{3.16}$$

which is higher than in the pure optically thin case. The emitted radiation is 'trapped' in the volume considered and, from the macroscopic point of view, the excited state is characterized by a lowered spontaneous emission rate, given by:

$$A_{21}^{\text{eff}} = A_{21}(1-J) \tag{3.17}$$

The factor $\eta = (1-J)$, commonly attributed to the probability for radiative escape from a cell (escape probability), exhibits in the case of low opacity and constant number density a direct dependence on the line broadening parameters, number density of the atoms in the lower state and the size of the cell. In summary, bearing in mind the basic assumption of spatially isotropic and frequently fully redistributed spontaneous emission, the J values for all three cases of geometry and three basic types of line profiles (Lorentzian, Voigt, Gaussian) discussed above are given by:

$$J \approx \begin{Bmatrix} R_S \\ 1.13 R_C \\ 0.64L \end{Bmatrix} \times \bar{N}_1 \times \frac{\pi e^2}{mc} f_{12} \times \begin{Bmatrix} 1/\pi\Delta_{\text{L}} \\ a_1^{\text{V}} P_{\text{V}}(0) \\ (2\ln2/\pi)^{1/2}/\Delta_{\text{G}} \end{Bmatrix}, \quad J \leq 0.3 \tag{3.18}$$

where the values for the coefficient a_1^{V}, which corresponds to the Voigt line profile, depend on the ratio $\Delta_{\text{L}}/\Delta_{\text{G}}$ and are in range between $1/2$ and $1/\sqrt{2}$.

3.3. The 'piece-by-piece' method

Among many approximations for the solution of the Holstein equation, a simple but efficient method for numerical solution is the so-called piecewise method [17]. The basic principle is to divide the vapor cell volume into n small optically thin regions with centers at corresponding $\vec{r}_{\text{cg}}^n$. The number density in the excited state is assumed to be constant within each region. Then, the specific trapping problem is defined by an n-dimensional set of linear equations with n unknown population densities $N_2(\vec{r}_{\text{cg}}^n)$. Obviously, this method fits with the concept of trapping adopted in Section 3.2. The substantial difference we make here is that we consider optically quasi-thin and slightly 'trapped' volumes. Using the results given in Section 3.2 it is instructive to examine the simplest case when we have two adjacent cubic volumes (see Fig. 4b) of equal size L, both relatively optical thin ($k_0^{\text{P}} L \leq 0.6$). In this 'piece-by-piece' approach, both volumes V_n and V_m are supposed to be under the same physical conditions (among others: $\bar{N}_1(n) = \bar{N}_1(m) = \bar{N}_1$). The volumes are excited by the pumping rates Π_n and Π_m and, as stand-alone units, are characterized by an effective spontaneous emission rate $A_{21}^{\text{eff}} = A_{21}(1-J_{\text{cub}})$. Then, following the scheme given by Eq. (3.6), with $A_{21} \to A_{21}^{\text{eff}}$, $\Delta V \to L^3$, $\left| \vec{r}_m - \vec{r}_n \right| \to L$ and $N_2(\vec{r}_i) \to \bar{N}_2(i)$, we obtain the system of two coupled relations for the average number densities $\bar{N}_2(n)$ and $\bar{N}_2(m)$:

$$A_{21}^{\text{eff}} \bar{N}_2(n) - A_{21}^{\text{eff}} L^3 \Phi \bar{N}_2(m) \approx \Pi_n \bar{N}_1 \tag{3.19}$$

$$-A_{21}^{\text{eff}} L^3 \Phi N_2(n) + A_{21}^{\text{eff}} \bar{N}_2(m) \approx \Pi_m \bar{N}_1$$

where, analogously to Eq. (3.7) and to the procedure performed in the steps from Eq. (3.10) to Eq. (3.15), the coupling factor Φ is given by:

$$\Phi = \frac{\int_\nu k(\nu) P(\nu) \exp[-k(\nu)L]}{4\pi L^2} \approx \frac{a_1^{\text{P}} k_0^{\text{P}} L}{4\pi L^3} = \frac{0.12 J_{\text{cub}}}{L^3}, \quad k_0^{\text{P}} L \leq 0.6 \tag{3.20}$$

Regarding the pumping of volumes V_n and V_m, we consider two cases. In the first case, when

(a) $\Pi_n = \Pi_m = \Pi$

the solution to Eq. (3.19) is:

$$\bar{N}_2(n) = \bar{N}_2(m)$$
$$\approx \frac{\Pi}{A_{21}(1-J_{\text{cub}})(1-0.12J_{\text{cub}})}\bar{N}_1 \qquad (3.21)$$

The above relation clearly shows that mutual influence between V_n and V_m (see Fig. 4b, left) leads to a further decrease in the effective spontaneous emission rate in the whole $V_n + V_m$ volume. In the second case, when

(b) $\Pi_n \neq 0$ and $\Pi_m = 0$

the following solutions for the number densities of the excited atoms in the particular volumes n and m are obtained:

$$\bar{N}_2(n) = \frac{\Pi_n}{A_{21}(1-J_{\text{cub}})(1-0.0144(J_{\text{cub}})^2)}\bar{N}_1$$
$$\approx \frac{\Pi_n}{A_{21}(1-J_{\text{cub}})}\bar{N}_1$$
$$(3.22)$$

$$\bar{N}_2(m) = \frac{0.12J_{\text{cub}}\Pi_n}{A_{21}(1-J_{\text{cub}})(1-0.0144(J_{\text{cub}})^2)}\bar{N}_1$$
$$\approx \frac{0.12J_{\text{cub}}\Pi_n}{A_{21}(1-J_{\text{cub}})}\bar{N}_1$$
$$(3.23)$$

Eq. (3.23) describes diffusion-like effects, i.e. widening of the originally excited zone by radiative transport (see Fig. 4b, right). In terms of optical pumping, it can also be described as the appearance of induced pumping in the medium outside of the primarily excited region.

The approach presented here yields a qualitative picture of the radiative transport in atomic vapors leading to the trapping and diffusion of the resonance radiation. With restraints for relatively optically thin cases acknowledged, these simple procedures enable quantitative treatment of the trapping effect as well, which is illustrated by an example in the following subsection.

3.4. Infinite cylinder: piece-by-piece approach

Trapping is a volume effect and, in its theoretical treatment by solving the Holstein equation, solu-tions were most often sought for two basic geom-etries studied originally by Holstein, i.e. the infinite cylinder and the infinite slab. In order to test the validity of the approximate solutions obtained here, we have applied the procedure described to an infinite cylinder.

For this purpose, we consider an infinite long cylinder with a radius R_C, which is divided into sub-regions of equal length $2R_C$ (see Fig. 4c). Each region is pumped by the same rate Π. By taking into account all assumptions made before, each sub-region n with the volume $V = 2\pi R_C^3$ can be characterized as a stand-alone unit by an effec-tive spontaneous emission rate $A_{21}^{\text{eff}} = (1-J_{\text{cyl}})A_{21}$, where $J_{\text{cyl}} \approx 1.13a_1^P k_0^P R_C$ for $k_0^P R_C \leq 0.35$ as given by Eq. (3.14). In the next step, we consider the piece-by-piece interaction between the sub-regions. The situation is described by an infinite system of coupled relations. Following Eq. (3.6) and the substitutions introduced in the previous subsection, the expression for the average number density $\bar{N}_2(n)$ of the n-th element is:

$$A_{21}^{\text{eff}}\big[\bar{N}_2(n) - 2V\Phi_1\bar{N}_2(n+1)$$
$$- 2V\Phi_2\bar{N}_2(n+2) - \ldots\big]$$
$$= \Pi\bar{N}_1(n) \qquad (3.24)$$

where, according to Eq. (3.7) and the approxima-tion mentioned above ($k_0^P R_C \leq 0.35$), the factors Φ_m are:

$$\Phi_m = \frac{\int_\nu k(\nu)P(\nu)\exp\big[-2mk(\nu)R_C\big]}{4\pi(2mR_C)^2}$$

$$\approx \frac{a_1^P k_0^P R_C}{8m^2(2\pi R_C^3)}\bigg[1 - (2mk_0^P R_C)\frac{a_2^P}{a_1^P}$$
$$+ \frac{(2mk_0^P R_C)^2}{2!}\frac{a_3^P}{a_1^P} - \frac{(2mk_0^P R_C)^3}{3!}\frac{a_4^P}{a_1^P} + \ldots\bigg] \qquad (3.25)$$

Using the values for the coefficients a_i^P given in Table 1, and fitting the series in Eq. (3.25) to an exponential function, we can write Φ_m as follows:

$$\Phi_m = \frac{a_1^P k_0^P R_C}{8m^2(2\pi R_C^3)} \exp\left[-2mk_0^P R_C/b^P\right] \qquad (3.26)$$

where the coefficient b^P for Lorentzian and Gaussian profiles are given by $b^L = 1.27$ and $b^D = 1.19$, respectively.

However, since equal pump rates for each volume element and homogeneous number density $\bar{N}_1(n) = \bar{N}_1(n+m) = \bar{N}_1$ are assumed, the problem is reduced to a single equation, because in that case $\bar{N}_2(n) = \bar{N}_2(n+m) = \bar{N}_2$ is valid. Thus, for an infinite cylinder Eq. (3.24) yields the following expression:

$$\bar{N}_2 = \frac{\Pi}{A_{21}(1-J_{cyl})(1-J'_{cyl})}\bar{N}_1 \qquad (3.27)$$

where

$$J'_{cyl} \approx \frac{1}{4}a_1^P k_0^P R_C \sum_{m=1}^{\infty} \frac{\exp\left[-2mk_0^P R_C/b^P\right]}{m^2},$$
$$k_0^P R_C \leq 0.35 \qquad (3.28)$$

Note that the series in Eq. (3.28) can be represented with great accuracy by the first three terms only. The approximate expression for the factor η, i.e. for the escape probability, is:

$$\eta_{cyl}^{\infty} \approx (1 - 1.13a_1^P k_0^P R_C)\Bigg(1 - \frac{1}{4}a_1^P k_0^P R_C$$
$$\times \sum_{m=1}^{\infty} \frac{\exp\left[-2mk_0^P R_C/b^P\right]}{m^2}\Bigg), \quad k_0^P R_C \leq 0.35$$
$$(3.29)$$

The values for η_{cyl}^{∞} calculated via Eq. (3.29) are shown in Fig. 5, together with the numerical calculations made by Post [21] for the same geometry. Both results are given for the case of a pure Doppler line profile. The numerical results published in [21] were obtained for values of $k_0^D R_C$ between 0.1 and 100. In that work, similar to the Holstein approximation, the solutions for the number density in the excited state were
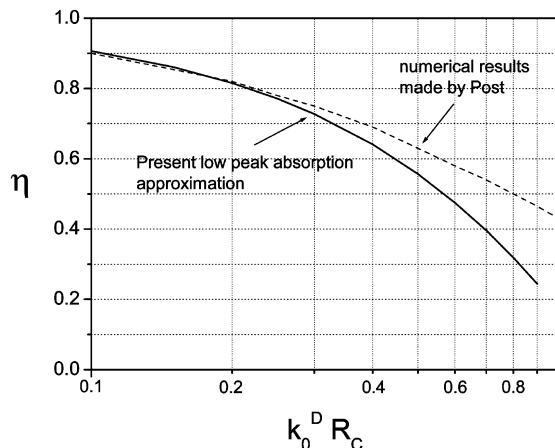

Fig. 5. The escape probability η calculated for the case of infinite cylindrical volume and Doppler broadened line as a function of the optical depth $k_0^D R_C$. The results of the approximation presented here are compared with the more general numerical calculations reported in [21].

expanded into power series and the escape probability was obtained by integration over the fundamental mode distribution. Post's calculations, as given in [20] show excellent agreement with experimental results. Very good agreement between the results obtained using Eq. (3.29) and the numerical results given in [21] for small values of $k_0^D R_C$ confirm the efficiency of the present piece-by-piece approach. This agreement is most probably the consequence of the equivalence of the physical assumptions made in the model presented here (uniform optical pumping, averaged constant number densities) and solving the Holstein equation for the fundamental mode distribution.
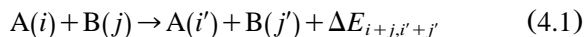
4. Collisional excitation energy transfer

Collisional excitation energy transfer (CEET) in thermal collisions between excited atoms and molecules in gases has been the subject of numerous investigations during the last decades. The CEET processes are important mechanisms for establishing the population distributions, and very often play a crucial role in many phenomena in excited gaseous media. Studies of such interactions are of great interest in a variety of fundamental and applied fields. Therefore, when speaking about

working schemes and the efficiency of atomic line filters, these non-radiative processes represent an inevitable issue.

4.1. Cross-sections for CEET processes

In general, the CEET processes involving two particles A and B excited to different states before and after collision can be schematically represented by:

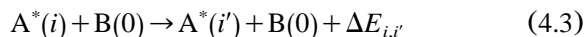$$A(i) + B(j) \rightarrow A(i') + B(j') + \Delta E_{i+j,i'+j'} \qquad (4.1)$$

where the energy defect $\Delta E_{i+j,i'+j'} = E_i + E_j - E_{i'} - E_{j'}$ is transferred to or gained from the kinetic energy of the colliding pair $A+B$. Studies on CEET concern the determination of rate coefficients or corresponding collision cross-sections for a particular reaction [Eq. (4.1)]. Denoting the states of the $A+B$ complex with $|1\rangle = |i,j\rangle$ and $|2\rangle = |i',j'\rangle$, the number of reactions $|1\rangle \rightarrow |2\rangle$ per unit volume and unit time is defined as the product $N_A(m)N_B(n)k_{12}$, where $N_A(m)$ and $N_B(n)$ are the number densities of colliding particles, and k_{12} [s^{-1} m^3] is the temperature-dependent rate coefficient. Analogously to the gas kinetic theory, the rate coefficient is usually defined as $k_{12} = \langle v \rangle Q_{12}$, where $\langle v \rangle$ is the average relative velocity of a colliding pair and the factor of proportionality Q_{12} [m^2] is the temperature-dependent collisional cross-section for the CEET process $|1\rangle \rightarrow |2\rangle$. In the same manner, we can define the cross-section Q_{21} for the reverse $|1\rangle \leftarrow |2\rangle$ process. These $Q_{ij}(T)$ cross-sections are averages of the actual cross-sections (see Section 4.2) over the thermal relative velocity distribution. In a statistical assembly in thermodynamic equilibrium and in the absence of other processes, a simple rate equation $N_A(i)N_B(j)k_{12} = N_A(i')N_B(j')k_{21}$ must be fulfilled. Since the number densities in that case obey the Boltzmann distribution, the principle of detailed balancing predicts that $Q_{12}(T)$ and $Q_{21}(T)$ should be in the ratio:

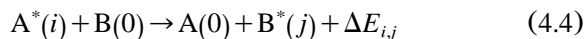$$Q_{12}(T)/Q_{21}(T) = (g_2/g_1)\exp(-\Delta E_{21}/kT) \qquad (4.2)$$

where the statistical weights of the $A+B$ system after and before CEET are labeled with g_i. This relation is a very sensitive check for the consistency of the experimental results and is very useful for the determination of complementary values for cross-sections in cases when only one member of the cross-section pair is known.
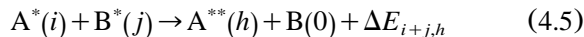
From the experimental and theoretical point of view, alkali atoms are the most convenient subjects for investigation of CEET processes, and therefore they are the most extensively studied systems in this field. An exhausting overview of the experimental and theoretical results up to 1974 is provided in [22,23]. The investigations of CEET in that earlier period are most frequently related to the excited alkalis in collisions with ground-state alkali atoms (of the same or a different type) or with noble gas atoms. Alkali atoms easily evaporate at relatively low temperatures and experiments were mainly performed in the temperature range of few 100 K above room temperature, which defines the collisions investigated as *thermal*. Low-pressure alkali vapors generated in cells at thermal equilibrium were optically excited by use of spectral lamps and the population densities in excited states were determined via fluorescence measurements. Here, two basic processes have been studied, known as intra-atomic mixing:

$$A^*(i) + B(0) \rightarrow A^*(i') + B(0) + \Delta E_{i,i'} \qquad (4.3)$$

and inter-atomic mixing:

$$A^*(i) + B(0) \rightarrow A(0) + B^*(j) + \Delta E_{i,j} \qquad (4.4)$$

The application of tunable lasers in later years enabled a large variety of precise experiments to be carried out and the investigation of processes in which two excited atoms in collision produce one atom excited in a high-lying state (h) and the other atom in the ground state:

$$A^*(i) + B^*(j) \rightarrow A^{**}(h) + B(0) + \Delta E_{i+j,h} \qquad (4.5)$$

These processes are known as energy pooling.

4.2. Elements of experimental approach

One of the simplest CEET experiment represents the resonance fine-structure mixing of the alkali

first $n^2P_{1/2}$ and $n^2P_{3/2}$ sublevels due to ground-state atoms of the same kind. The first alkali resonance doublets lie isolated in the energy term diagram, and, for example, if the $n^2P_{3/2}$ is optically excited from the ground-state $n^2S_{1/2}$, the rate equations for the states $n^2P_{1/2}$ and $n^2P_{3/2}$ can be written as:

$$\frac{dN_1}{dt} = -N_1 A_{10} - N_1 R_{12} + N_2 R_{21} \qquad (4.6)$$

$$\frac{dN_2}{dt} = +N_1 R_{12} - N_2 A_{20} - N_2 R_{21} + \Pi_{02} N_0 \qquad (4.7)$$

where the states $n^2S_{1/2}$, $n^2P_{1/2}$ and $n^2P_{3/2}$ are labeled with indices 0,1,2, while R_{12} and R_{21} are the collision transfer rates of the form $R_{ij} = k_{ij}N_P = \langle v \rangle Q_{ij}N_A$. In the case of cw laser excitation, i.e. in the steady-state regime, the ratio of the indirectly N_1^{ind} to directly produced N_2^{dir} number density yields via Eq. (4.6) the relationship $N_1^{ind}/N_2^{dir} = R_{21}/(A_{10} + R_{12})$. Analogously, for optically pumped $n^2P_{1/2}$, we obtain $N_2^{ind}/N_1^{dir} = R_{12}/(A_{20} + R_{21})$. With known values for the radiative relaxation rates, these data pairs yield the values for collision transfer rates. Finally, to evaluate the corresponding cross-sections, the values for the average relative velocity and the perturber number density are needed. Although this may appear to be a relatively simple task to accomplish, due to several difficulties it is not. First, determination of the ground-state number densities for alkalis is often difficult. Furthermore, to achieve detectable signals the experiments often have to be performed at ground-state number densities where, due to radiation trapping, measured lifetimes are no longer natural lifetimes and the determination of effective lifetimes is necessary. Once effective lifetimes are involved, diffusion of the excited atoms out of the excitation zone has to be considered too. Several additional effects, for example fluorescence anisotropy due to polarization, have to be properly taken into account. The situation becomes more complicated in systems in which simple two-level models are not appropriate and the set of relevant rate equations should be enlarged. It usually takes several experiments, performed independently by different groups, to establish reliable cross-section values for a particular CEET.

4.3. Elements of theoretical approach

The comparison of experimental and theoretical results provides an important check on our understanding of the dynamics of inelastic collisions in gases and our knowledge of interaction potentials between colliding atoms or molecules. The problem of theoretical determination of CEET cross-sections basically consists of the determination of non-radiative quantum-mechanical transition probabilities between the initial and final states of a A+B collision complex. Due to their hydrogen-like electronic structure and long-range electrostatic interaction potentials, alkali–alkali collisional systems seem to be ideal subjects for theoretical modeling of CEET processes.

Parallel to the CEET studies during the last decades, many investigations in a closely related field of collisional broadening of spectral lines were conducted. In these investigations, alkali–alkali and alkali–noble gas systems were also extensively studied. Numerous spectral line-shape measurements [24] and calculations of adiabatic interatomic potentials, i.e. the atomic potentials with the atoms at rest, have been performed, yielding a relatively clear, but certainly not simple pictures of the relationships between collisional line-broadening parameters and interatomic potentials. As for cesium–cesium interaction potentials, most relevant information can be found in references [25–29]. Regarding collisional dynamics, typical physical conditions in CEET experiments are very convenient for the application of several standard quantum-mechanical approximate procedures. First, the mean relative velocities of colliding atoms (typically in the range between 10^4 and 10^5 cm s^{-1}) are obviously negligible in comparison with the velocity of optical electrons (approx. 10^8 cm s^{-1}) which, in terms of quantum mechanics, means that the collisions are *slow*, and the motion of nuclei and electrons can be regarded separately (adiabatic approximation). Furthermore, the de Broglie wavelength for the relative motion of the colliding complex (in CEET experiments typically 10^{-9} cm) is substantially smaller than

the range parameter of the interaction potentials (typically up to 10^{-8} cm for alkali–alkali interactions), which defines the collisions as *quasiclassical*. In this case, the motion of the colliding nuclei can be described by classical trajectories $\vec{r} = \vec{r}(\vec{v},t)$. In a simplified model, we can regard the collisional trajectories as straight lines with constant velocity $\vec{v}$. In this case the internuclear separation is $r = R\sqrt{1 + v^2 t^2/R^2}$, where R is the distance of closest approach of the colliding particles (impact parameter). Interatomic potentials, vanishing at infinite nuclear distances, are generally represented with terms proportional to $1/r^n$ (resonance dipole–dipole interaction, $n=3$; van der Vaals interaction, $n=6$, etc.). As a function of time, these interactions are of a bell-shaped form and their maximum occurs approximately during the collision time $\tau_c \approx R/v$. Taking into account the mean relative velocities under typical conditions in CEET experiments, τ_c is significantly shorter than the atomic radiative lifetimes. Therefore, all excited states can be regarded as stable during a single collision. In addition, at typical atom number densities (up to 10^{18} cm^{-3}) the collisions are separated in time, i.e. only binary collisions have to be taken into account.

Following the simple two-state model described by Eqs. (4.6) and (4.7), states 1 and 2 at infinite r, i.e. at the beginning of the collision, can be represented by an orthonormal set of stationary eigenfunctions $|1\rangle$ and $|2\rangle$ of a time-independent Hamiltonian operator $\hat{H}_0$ with eigenvalues E_1^0 and E_2^0, which is related to the unperturbed quantum-mechanical system A+B. During the collision in the time interval $(t = -\infty, t = +\infty)$, an interatomic perturbation $\hat{V}$ represented by terms of the form $\hat{V}^{(n)} = \hat{C}^{(n)}/r^n(\vec{v},t)$ occurs, and the perturbed Hamiltonian becomes time-dependent $\hat{H} = \hat{H}_0 + \hat{V}$. Here, $\hat{C}^{(n)}$ is the operator for the particular type of interaction, which is related to the coordinates of the valence electrons. In accordance with the common quantum-mechanical procedure, the wavefunction $|\Psi\rangle$ of the collisional system obeying the time-dependent Schrödinger equation $i\hbar d|\Psi\rangle /dt = (\hat{H}_0 + \hat{V}) \times |\Psi\rangle$ can be represented in the form of a linear combination $|\Psi\rangle = a_1(t)|1\rangle + a_2(t)|2\rangle$. Applying the orthonormal properties of the unperturbed states to the time-dependent Schrödinger equation, we obtain the time development of the system considered, described by two coupled differential equations for the time-dependent coefficients $a_k(t)$:

$$i\hbar \frac{da_1}{dt} = a_1 V_{11} + a_2 V_{12} \exp(-i\Delta E_{21} t/\hbar) \qquad (4.8)$$

$$i\hbar \frac{da_2}{dt} = a_1 V_{21} \exp(i\Delta E_{21} t/\hbar) + a_2 V_{22} \qquad (4.9)$$

where the matrix elements are briefly written as $V_{ij} = \langle i|\hat{V}|j\rangle$. Considering the system being in the higher state $|2\rangle$ before collision, i.e. with initial conditions $a_1(t = -\infty) = 0$ and $a_2(t = -\infty) = 1$, this equation system corresponds to the set of Eqs. (4.6) and (4.7), where the upper state 2 is pumped. The probability of finding the collisional pair after collision in state $|1\rangle$ depends on the relative velocity and the parameters of the collisional trajectory, and is given by $P_{21}(R,v) = |a_1(R,v,t = +\infty)|^2$.

4.4. Comparing theory with experiment

To compare the theoretical results with the experimentally obtained values for the cross-sections, we should carry out appropriate integrations over the collision parameters of the collision trajectories and average over the velocity distribution corresponding to the physical conditions of the particular experiment. If the energy defect ΔE is negligible in comparison with the mean kinetic energy of the collision system, we can suppose that the velocities remain constant during the collision and the collision trajectories can be represented by straight lines. Then, the velocity-dependent cross-section is given by integration over the impact parameters as follows:

$$\sigma_{21}(v) = 2\pi \int_0^\infty R P_{21}(R,v,t = +\infty)\, dR \qquad (4.10)$$

Since the measurable quantity in experiments is the rate coefficient k, the corresponding value for the velocity-averaged cross-section should be calculated as $Q_{21} = \langle v\sigma_{21}(v)\rangle/\langle v\rangle$. Assuming the Maxwell–Boltzmann velocity distribution $P(v,T) = v^2\exp[-\mu v^2/kT]$, where μ is the reduced mass of the collision pair, we obtain the following relation for the exothermic temperature-dependent cross-section:

$$Q_{21}(T) = \frac{\int_0^\infty \sigma_{21}(v)v^3\exp[-\mu v^2/2kT]\ dv}{\int_0^\infty v^3\exp[-\mu v^2/2kT]\ dv}$$

(4.11)

Under the assumptions made above, the same relation holds for the cross-section Q_{12} of the inverse endothermic collision. If the energy defect is not negligible in comparison with the mean kinetic energy, the situation becomes more complicated and enters the field of velocity-changing collisions. In this case the collision trajectories cannot be represented by simple straight lines. As for the cross-section related to the endothermic reactions, in such cases the lower limit of the integral in the nominator of Eq. (4.11) should be replaced by a threshold value $v_{\mathrm{th}} = \sqrt{2\Delta E/\mu}$.

Different from the field of collision line broadening, the agreement between experimental and theoretical results is rather poor in CEET. In spite of the many conveniences mentioned for the theoretical treatment of CEET processes involving alkali atoms, theoretical determination of the corresponding cross-sections is extremely complicated. Since the interactions in collisions remove the degeneracy of the states investigated, a large number of sub-states should be considered. The collision dynamics is generally very complex and can hardly be represented by straight-line trajectories with constant velocity. Solution of the corresponding multidimensional set of coupled time-dependent differential equations requires complicated time-consuming numerical calculations, e.g. as shown in [30]. These calculations yield good agreement with experimental results, but their complexity and specific parameters make it difficult to obtain transparent insight into the importance of special mechanisms leading to a particular CEET. On the other hand, numerous models have been proposed to simplify calculation of the CEET cross-sections and to obtain tractable analytical expressions that yield a better insight into the collision transfer mechanisms. It is typical for these models [23,31,32] to concern the transitions probabilities $P(R,\vec{v})$ localized in narrow regions ΔR around the characteristic impact parameters R_0. Here, the basic assumption is that the off-diagonal matrix elements in the system of Eqs. (4.8) and (4.9) are small compared with the difference between the diagonal ones. Then, in such case of generally weak coupling, the non-radiative transitions between the initial and final states becomes significant only in narrow regions around the pseudo-crossing points (located at R_0) of the quasi-molecular adiabatic potential curves, where the well-known Landau–Zener approach [33] can be applied. Such models yield various analytical expressions among the basic CEET parameters, which makes it easier to interpret the relevant transfer mechanisms, but unfortunately the numerical results obtained are systematically and often significantly lower than the experimental data.

4.5. CEET cross-sections for some alkali–alkali systems

In general, the magnitude of collision cross-sections depends on the kind of collision partners, the configuration of the initial and final states, the energy defect and the temperature. Owing to the body of available experimental cross-section data, certain regularities with respect to the dependence on energy defect and temperature can be discerned. As an example, two data sequences are given in Table 2. The first concerns the fine-structure mixing of the first resonance n^2P_J states of Na, K, Rb and Cs due to collisions with ground-state atoms of the same species. The experimental values cited were obtained at different temperatures in the range between 323 and 573 K. The second set of the values constitutes the data for the fine-structure mixing of resonance n^2P_J states of Li, Na, K and

Rb in collisions with ground-state Cs atoms. These data were measured at similar temperatures of approximately 500 K. It is instructive to inspect the behavior of the cross-sections for the exothermic reactions, which, in contrast to endothermic ones, do not have a velocity threshold. The data for the exothermic cross-sections, depicted in Fig. 6, show clear and almost identical dependence on the reaction energy defect. Presented in a double logarithmic scale, the cross-sections decrease approximately as $1/\Delta E$, with the cross-sections for the homonuclear processes being shifted towards higher values. This shift seems to be plausible, because the homonuclear $A^* + A$ reactions are characterized by strong long-range dipole–dipole resonance interactions [23,34–36], while the CEET in heteronuclear $A^* + Cs$ systems is found to be due to electrostatic interactions of shorter range, i.e. due to dipole–quadrupole interactions [37–41] in the cases at hand. As for the temperature dependence of the exothermic cross-sections measured, the cross-sections considered show a moderate decrease with increasing temperature.

The relationship between the exothermic cross-sections and the energy defect in homonuclear alkali–alkali collisions had been noticed in the earliest CEET investigations [22]. Similar behavior
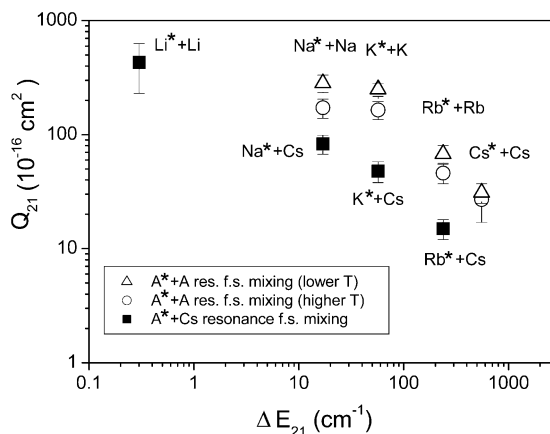

Fig. 6. The cross-sections, listed in Table 2, for the $n^2P_{3/2} \rightarrow n^2P_{1/2}$ fine-structure mixing of the first resonance states in alkalis induced by collisions with the ground-state atoms of like or unlike species, plotted as a function of the reaction energy defect. The data depicted were obtained at different temperatures in the range between 323 and 573 K. The circles and triangles, representing the $A^* + A$ processes, label the values obtained at higher and lower temperature, respectively.

was also observed for the energy pooling processes [42]. The regularity of the $Q \sim 1/\Delta E$ dependence for homonuclear and heteronuclear alkali–alkali reactions has been recently investigated in detail

Table 2

Cross-sections for homonuclear and heteronuclear fine-structure mixing in alkalis: the cross-sections for the fine-structure mixing of the first resonance n^2P_J states of Na, K, Rb and Cs by collisions with the ground-state atoms of the same species and the cross-sections for the fine-structure mixing of the first resonance n^2P_J states of Na, K and Rb induced by collisions with Cs in the ground state

Process	Q_{12} (10^{-16} cm^2)	Q_{21} (10^{-16} cm^2)	T (K)	Reference
Homonuclear $A^* + A$				
Na $(3p_{1/2})$ + Na Na $(3P_{3/2})$ + Na	532 ± 80	283 ± 42	424	[22]
	330 ± 60	330 ± 30	573	[34]
K $(4P_{1/2})$ + K K $(4P_{3/2})$ + K	370 ± 74	250 ± 50	350	[22]
	330 ± 66	165 ± 33	550	
Rb $(5P_{1/2})$ + Rb Rb $(5P_{3/2})$ + Rb	53 ± 11	68 ± 14	360	[22]
	74 ± 15	46 ± 9	543	
Cs $(6P_{1/2})$ + Cs Cs $(6P_{3/2})$ + Cs	6.4 ± 1.3	31 ± 6	323	[22]
	14 ± 5	27 ± 10	585	[36]
Heteronuclear $A^* + Cs$				
Li $(2P_{1/2})$ + Cs Li $(2P_{3/2})$ + Cs	890 ± 400	430 ± 193	475	[38]
Na $(3P_{1/2})$ + Cs Na $(3P_{3/2})$ + Cs	140 ± 28	83 ± 17	530	[39]
K $(4P_{1/2})$ + Cs K $(4P_{3/2})$ + Cs	77 ± 15	48 ± 10	520	[40]
Rb $(5P_{1/2})$ + Cs Rb $(5P_{3/2})$ + Cs	16.5 ± 3.3	15 ± 3	575	[41]

[43], but an adequate, general theoretical description of this phenomenon is still lacking. Nevertheless, regular behavior with respect to a given characteristic parameter, for instance the energy defect, of the CEET cross-sections measured, can be useful in making an estimation of the cross-sections for those processes that have not yet been investigated.

4.6. CEET processes in Cs*+Ar,He mixtures

Since many experiments on imaging filters [5–10] were performed in Cs–Ar systems, the CEET processes in mixtures of optically excited cesium atoms and ground-state argon atoms are of particular interest here. Expected CEET reactions occurring in a mixture of excited cesium atoms and ground-state noble gas atoms are those involving the following collision pairs: Cs*+Cs, Cs*+Cs*, Cs*+noble gas and Cs*+Cs$_2$. Based on data published in the literature, it is possible to form a scheme for the thermal cross-section dependence on the energy defect and temperature for a given class of collisions. For comparison, as well as for confirmation of the regularities noticed in the cross-section behavior, data for some other alkalis

and noble gases are also given. All data presented here were obtained by measurements in cells at thermal equilibrium.

4.6.1. CEET involving two cesium atoms

As pointed out in the previous section, the behavior of the exothermic cross-sections is more instructive than that of the endothermic ones, since the latter depend on the reaction threshold, which introduces an additional proportionality factor equal to $e^{-\Delta E/kT}$. The cross-sections for various exothermic CEET processes involving two cesium atoms have been collected from the available literature, were sorted by reaction type and are listed in Tables 3a, 3b and 3c, where the data for intra-multiplet mixing, inter-multiplet mixing and energy pooling processes are given, respectively. For some of the processes listed, the cross-section was measured only for the corresponding endothermic reaction, and the values listed for exothermic processes were calculated using the principle of detailed balancing; these results are listed in Table 3a–c in braces.

The data collected in Table 3a–c were measured in the temperature range between 350 and 600 K.

Table 3a
Cross-sections for intra-multiplet nP$_{3/2} \rightarrow n$P$_{1/2}$ and nD$_{5/2} \rightarrow n$D$_{3/2}$ mixing in cesium induced by collisions with ground-state Cs atoms

Number	Cs (2)+Cs (6S) → Cs (1)+Cs (6S)	ΔE_{21} (cm^{-1})	T (K)	Q_{21} (10^{-16} cm^2)	Reference
1	Cs (6P$_{3/2}$) → Cs (6P$_{1/2}$)	554	350	31±3	[35]
			585	27±10	[36]
2	Cs (7P$_{3/2}$) → Cs (7P$_{1/2}$)	181	443	107±22	[48]
3	Cs (8P$_{3/2}$) → Cs (8P$_{1/2}$)	83	420	{126±38}	[44]
4	Cs (5D$_{5/2}$) → Cs (5D$_{3/2}$)	98	601	36±8	[45]
			585	57±19	[46]
5	Cs (6D$_{5/2}$) → Cs (6D$_{3/2}$)	43	413–533	210±40	[47]
6	Cs (7D$_{5/2}$) → Cs (7D$_{3/2}$)	21	413–533	270±50	[47]
7	Cs (8D$_{5/2}$) → Cs (8D$_{3/2}$)	11.7	413–533	600±120	[47]
8	Cs (9D$_{5/2}$) → Cs (9D$_{3/2}$)	7.2	413–533	1260±270	[47]
9	Cs (10D$_{5/2}$) → Cs (10D$_{3/2}$)	4.7	413–533	2020±400	[47]
10	Cs (11D$_{5/2}$) → Cs (11D$_{3/2}$)	3.25	398–453	5500±1700	[49]
11	Cs (12D$_{5/2}$) → Cs (12D$_{3/2}$)	2.3	398–453	8700±2600	[49]
12	Cs (13D$_{5/2}$) → Cs (13D$_{3/2}$)	1.7	398–453	11400±3400	[49]

For the processes where the cross-section was originally measured only for the endothermic reaction, the corresponding cross-section for the exothermic process was obtained from the principle of the detailed balancing and these values are given in braces. The reaction energy defect and the experimental temperature are given. References are in square brackets.

Table 3b
Cross-sections for various inter-multiplet $nl \rightarrow n'l'$ mixing processes in cesium induced by collisions with ground-state Cs atoms

Number	Cs (2) + Cs (6S) → Cs (1) + Cs (6S)	ΔE_{21} (cm^{-1})	T (K)	Q_{21} (10^{-16} cm^2)	Reference
1	Cs (5D) → Cs (6P)	3010	480–637	30±3	[45]
			585	35±10	[46]
2	Cs ($7D_{3/2}$) → Cs ($8P_{1/2}$)	339	420	{33±8}	[44]
3	Cs ($7D_{5/2}$) → Cs ($8P_{1/2}$)	360	420	{23±6}	[44]
4	Cs (4F) → Cs (8S)	155	525	{185±60}	[22]
5	Cs ($8P_{3/2}$) → Cs (8S)	1475	525	{120±40}	[22]
6	Cs (9D) → Cs (8D)	1013	440	121±50	[50]
7	Cs (9D) → Cs (10S)	536	440	28±14	[50]
8	Cs (9D) → Cs (6F)	507	440	110±55	[50]
9	Cs (10D) → Cs (8D)	1657	440	111±45	[50]
10	Cs (10D) → Cs (6F)	1139	440	144±72	[50]
11	Cs (10D) → Cs (9D)	636	440	212±85	[50]
12	Cs (10D) → Cs (11S)	338	440	30±15	[50]
14	Cs (10D) → Cs (7F)	320	440	162±81	[50]
15	Cs (11D) → Cs (10D)	428	440	{128±53}	[50]
16	Cs (7F) → Cs (9D)	312	440	{169±85}	[50]
17	Cs (11S) → Cs (9D)	294	440	{273±136}	[50]
18	Cs (8F) → Cs (10D)	210	440	{227±114}	[50]
19	Cs (12S) → Cs (10D)	198	440	{285±143}	[50]
20	Cs (6P) → Cs (6S)	11548	635	1.6±1.4	[36]
			480–637	2.1±1	[51]

Legend as for Table 3a.

Table 3c
Cross-sections for a series of energy pooling processes in cesium vapor

Number	Cs (i) + Cs (j) → Cs (i') + Cs (j')	$\Delta E_{i+j,i'+j'}$ (cm^{-1})	T (K)	Q_{21} (10^{-16} cm^2)	Reference
1	Cs (6P) + Cs (6P) → Cs (6D) + Cs (6S)	447	570	190±57	[52]
2	Cs (6P) + Cs (5D) → Cs (7D) + Cs (6S)	45	570	560±225	[52]
3	Cs (7F) + Cs (6S) → Cs (5D) + Cs (5D)	32	570	{1160±460}	[52]
4	Cs (6D) + Cs (6S) → Cs ($6P_{1/2}$) + C ($6P_{1/2}$)	258	600	{163±65}	[53]
5	Cs ($6P_{1/2}$) + Cs ($6P_{3/2}$) → Cs (6D) + Cs (6S)	296	600	70±56	[53]
6	Cs ($6P_{3/2}$) + Cs ($6P_{3/2}$) → Cs (6D) + Cs (6S)	850	600	<70	[53]
			350	83±37[a]	[54]
7	Cs ($6D_{3./2}$) + Cs (6S) → Cs ($6P_{1/2}$) + Cs ($6P_{1/2}$)	232	337–365	{168±40}	[54]
8	Cs ($6D_{5./2}$) + Cs (6S) → Cs ($6P_{1/2}$) + C ($6P_{1/2}$)	275	337–365	{82±40}	[54]
9	Cs ($6P_{3/2}$) + Cs ($6P_{3/2}$) → Cs ($6D_{3./2}$) + Cs (6S)	876	337–365	27±9	[54]
10	Cs ($6P_{3/2}$) + Cs ($6P_{3/2}$) → Cs ($6D_{5./2}$) + Cs (6S)	833	337–365	56±28	[54]

Legend as for Table 3a.
[a] Obtained from J-selective cross-section for the Cs ($6P_{3/2}$) + Cs ($6P_{3/2}$) → Cs ($6D_J$) + Cs ($6S_{1/2}$) processes reported in [54].

In Section 4.7 it is shown that cross-sections of the order of magnitude of 10^{-16} cm^2 or higher exhibit weak dependence on temperature. Therefore, it is suitable to plot the listed cross-sections vs. energy defect ΔE, as shown in Fig. 7. It can be observed that all data, regardless of the type of process, lie around straight lines with the same slope of $\sim 1/\Delta E$. The straight lines differ only in magnitude, depending on the particular CEET process. This behavior is more apparent if only the data for intra-multiplet mixing and energy pooling are compared. As for the inter-multiplet
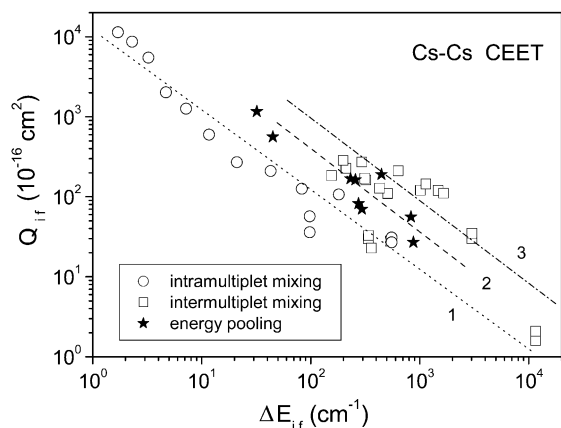
Fig. 7. The cross-sections for various exothermic CEET processes involving two cesium atoms (listed in Table 3a–c) plotted against the energy defect ΔE for the reaction. The straight lines labeled with 1, 2 and 3 through the sets of the data listed in Table 3a,c,b, respectively, are only guides for the eye.

mixing, the data scatter but still fit the general picture.

It should be emphasized that the behavior of the cross-sections presented for the CEET in Cs + Cs systems shows a picture very similar to that given in reference [43], where a set of exothermic cross-sections for a series of alkali–alkali interactions is presented as a function of the energy defect. It is far beyond the scope of this paper to propose an explanation for the general $Q \sim 1/\Delta E$ relation for CEET involving alkalis. There are also some data that deviate from the general trend (illustrated in Fig. 7 here, as well as in reference [43]). These deviations can be attributed either to possible systematical experimental errors, which are frequent in this field, or a specific theoretical explanation may be found for the disagreement with the general trend. However, such an empirical picture enables an estimation of at least the order of magnitude of the unknown cross-sections, which might be helpful in some applications.

4.6.2. CEET involving excited Cs and ground-state noble gas atoms

Excitation transfer between alkali states due to interaction with noble gases can easily be detected and there is a long history of such experiments

[22]. Here, the fine-structure mixing of the lowest alkali states was studied most frequently. In the case of the Cs first resonance level, which is very important in many working excitation schemes, there are unclear points in the literature, which are addressed in the following text.

For the cesium $6^2P_{1/2} \leftrightarrow 6^2P_{3/2}$ excitation transfer due to inert-gas collisions, two pioneering works are still most relevant. In the first, Czajkowski et al. [55] measured cross-sections for the fine-structure mixing of Cs $6P_J$ states induced by collisions with He, Ne, Ar, Kr and Xe at the constant temperature $T = 311$ K. In the second [56], Gallagher reported extensive studies of Cs $6P_J$ and Rb $5P_J$ mixing due to noble gases. In Gallagher's work the temperature dependence of CEET cross-sections for $Cs^* + He$, Ne and $Rb^* + He$, Ne, Ar, Kr, Xe were measured in the temperature range between 300 and 900 K. The exothermic cross-sections were found to have a strong temperature dependence ($\sim T^2$), i.e. strong dependence on the average relative velocity ($\sim \langle v \rangle^4$).

Due to the cross-section velocity dependence observed in [56], we can expect an approximate relationship $Q \sim 1/\mu^2$ to hold. Therefore, to compare the data of [55] and [56] it seems suitable to plot these results as a function of the reduced mass μ of the particular collision partner. In Fig. 8a, the data for $Cs^* + X$ (X = noble gas) collisions given in [55] and data for the $Cs^* + He$, Ne cases at 311 K taken from [56] are plotted on a double logarithmic scale against μ_{Cs-X}. These cross-sections are extremely small in comparison with typical values for alkali–alkali collisions. Adequate theoretical modeling for the $Cs^* + $ noble-gas collision cross-sections can be found in [23]. As can be observed in Fig. 8a, the results of [55,56] for the fine-structure mixing due to helium are in reasonable agreement. In addition, the ratios Q_{12}/Q_{21} are approximately 0.15 at $T = 311$ K, as predicted by the principle of detailed balancing. The data given in [56] for the $Cs^* + Ne$ case also show the agreement with the principle of detailed balancing, but they are more than one order of magnitude smaller than those reported in [55]. In contrast to that, the paper [55] reports data sets for $Cs^* + Ne$, Ar, Kr, Xe, which indicate a breakdown of the
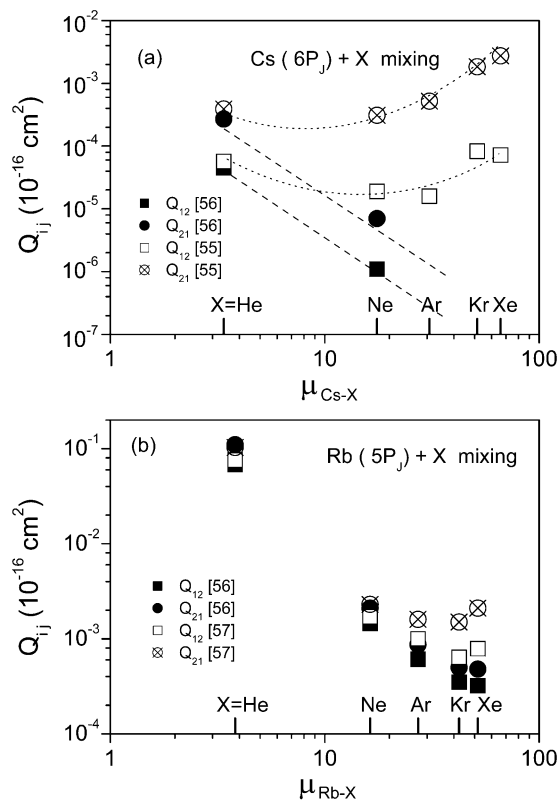
Fig. 8. (a) The cross-sections for the cesium 6 ^2P_J excitation transfer due to inert-gas collisions plotted in a double logarithmic scale against the reduced mass μ_{A-X} of the collision partners (X = He, Ne, Ar, Kr, Xe).The numbers in square brackets are the corresponding references. The data [56] were taken from the reported Q vs. T curve at $T = 311$ K. The data [55] were measured at $T = 311$ K. (b) The same as in (a), but for the rubidium 5 ^2P_J excitation transfer. The data [56] were taken from the reported Q vs. T curve at $T = 340$ K. The data [57] were measured at $T = 340$ K.

principle of detailed balancing. A similar situation can also be found in the case of Rb $5P_J$ fine-structure mixing by noble gas collisions, which was investigated in [56,57]; a comparison of these data is made in Fig. 8b.

As pointed out in [56], significant deviations from the principle of detailed balancing in [55,57] are due to systematic errors in the measurement of Q_{21} values, caused by the far wing line broadening of the alkali D lines. The broadened wings, which depend linearly on the noble gas density, leaked

through fairly broad interference filters centered on the D lines and gave rise to intensity contributions in the transfer cross-section measurements. However, only the Q_{21} cross-section measurements were affected because the far wing line broadening of the alkali resonance lines is asymmetric. For the reason mentioned, the Q_{21} values reported in [55,57] were disregarded in later review articles [22], while the Q_{12} data of [55,57] were still cited.

However, as shown in Fig. 8a, the Q_{12} value of [55] for Ne is more than one order of magnitude higher than the same datum found in [56]. Extrapolation of the results of [56] would suggest even stronger discrepancies for heavier noble gases. As pointed out in [56], the cross-sections for the Cs–noble-gas collisions are extremely small ($< 10^{-22}$ cm^2, with the exception of helium), in which case a polyatomic impurity concentration in the inert gas of one part in 10^7 could overshadow the doublet transfer measured. It was observed that even 6.0-grade Ne produced excessive cross-sections against Cs if used before additional cleaning. The experiments in [56] were not continued to Cs*–Ar, Kr or Xe, because of the time necessary to perform the cleaning procedure. Accordingly, it is most likely that molecular impurities in the inert gas contributed to the large Q_{12} cross-sections observed by the authors in [55]. In this case the correct mixing cross-sections for Cs $6P_J$ by argon at room temperature should be approximately 10^{-22} cm^2, as indicted in Fig. 8a.

Bearing in mind these facts and returning to the Cs* + Ar resonance fine-structure mixing, it is amazing that the cross-section for the Cs $6P_{1/2} \rightarrow$ Cs $6P_{3/2}$ transfer induced by collisions with argon given in [55] is still the only experimental value to be found in the literature. We think that it is useful to draw the attention of the reader to the fact that the results of [55], both for Q_{12} and Q_{21}, can be found cited even in recent [17] literature without appropriate discussion.

The data for CEET exothermic cross-sections in Cs* + Ar reactions taken from the literature are listed in Table 4. For comparison, data for the Cs* + He collisions are also collected and listed in Table 5. As for the Cs $7P_J$ fine-structure mixing by inert gases, systematic measurement of the

Table 4
Cross-sections for intra-multiplet $nP_{3/2} \to nP_{1/2}$, $nD_{5/2} \to nD_{3/2}$ and inter-multiplet $nl \to n'l'$ mixing in cesium induced by collisions with argon

Number	Cs (2) + Ar → Cs (1) + Ar	ΔE_{21} (cm^{-1})	T (K)	Q_{21} (10^{-16} cm^2)	Reference
Intramultiplet mixing					
1	Cs ($6P_{3/2}$) → Cs ($6P_{1/2}$)	554	311	{5.2×10^{-4}}[a]	[55]
				2×10^{-6}[b]	[56]
2	Cs ($7P_{3/2}$) → Cs ($7P_{1/2}$)	181	405	0.072 ± 0.02	[58]
			630	0.180 ± 0.04	[58]
			450	0.10 ± 0.02	[59]
			615	0.17 ± 0.03	[59]
3	Cs ($8P_{3/2}$) → Cs ($8P_{1/2}$)	83	420	{3.6 ± 1.1}	[44]
			620	{4.2 ± 1.3}	[44]
4	Cs ($8D_{5/2}$) → Cs ($8D_{3/2}$)	11.7	360	{133 ± 21}	[60]
5	Cs ($9D_{5/2}$) → Cs ($9D_{3/2}$)	7.2	360	{150 ± 27}	[60]
6	Cs ($10D_{5/2}$) → Cs ($10D_{3/2}$)	4.7	353	{211 ± 42}	[61]
7	Cs ($11D_{5/2}$) → Cs($11D_{3/2}$)	3.25	353	{263 ± 54}	[61]
8	Cs ($12D_{5/2}$) → Cs ($12D_{3/2}$)	2.3	353	{262 ± 67}	[61]
9	Cs ($13D_{5/2}$) → Cs ($13D_{3/2}$)	1.7	353	{268 ± 80}	[61]
10	Cs ($14D_{5/2}$) → Cs($14D_{3/2}$)	1.3	353	{260 ± 80}	[61]
Intermultilplet mixing					
1	Cs ($7D_{3/2}$) → Cs ($8P_{1/2}$)	339	420	{0.46 ± 0.14}	[44]
2	Cs ($7D_{5/2}$) → Cs ($8P_{1/2}$)	360	420	{0.33 ± 0.10}	[44]
3	Cs ($6D_{3/2}$) → Cs ($7P_{3/2}$)	642	450	{0.029 ± 0.009}	[59]
4	Cs ($6D_{3/2}$) → Cs ($7P_{1/2}$)	823	450	{~ 0.014}	[59]

For the processes where the cross-section was originally measured only for the endothermic reaction, the corresponding cross-section for the exothermic process was obtained from the principle of the detailed balancing. These values are given in braces. The reaction energy defect and the experimental temperature are indicated and the original references are given in square brackets.

[a] The value calculated using the principle of the detailed balancing and the value for the endothermic cross-section for the process, which probably includes contributions due to molecular impurities (see text).

[b] The hypothetical value suggested by measurements reported in [56].

cross-sections in the temperature range between 405 and 630 K is presented in [58]. There is very good agreement between these results and the data obtained at two other temperatures (450 and 615 K) reported in [59]. Similar to Cs $6P_J$, the data for Cs $7P_J$ mixing due to He are significantly (approx. two orders of magnitude) larger than for other noble gases. A rapid variation of the exothermic cross-sections with temperature (approx. T^2) was observed in the cases of Ne, Ar and Kr, while for Xe and especially for He, the temperature dependence was less pronounced. The remainder of the data listed in Tables 4 and 5 are mainly related to the inter-multiplet mixing of higher nP_J and nD_J states. There are also a few data for nP–nD inter-multiplet mixing. Unfortunately, all these data were originally measured only for the endothermic processes and the values for the exothermic cross-sections were calculated by applying the principle of detailed balancing.

The data given in Tables 4 and 5 are plotted on a double logarithmic scale vs. energy defect in Fig. 9a,b, respectively. As can be observed for the $Cs^* + Ar$ and $Cs^* + He$ cases, the data for nP_J and nD_J intra-multiplet mixing can be fitted to a continuous function of the energy defect, while the data for inter-multiplet mixing obviously belong to the other, higher-lying data sets. Explanations for the saturation and the decrease in cross-section values in the ΔE zero limit for the Ar and He cases can be found in the corresponding references.

Table 5
The cross-sections for intra-multiplet $n\mathrm{P}_{3/2} \rightarrow n\mathrm{P}_{1/2}$, $n\mathrm{D}_{5/2} \rightarrow n\mathrm{D}_{3/2}$ and inter-multiplet $nl \rightarrow n'l'$ mixing in cesium induced by collisions with helium

Number	Cs (2) + He → Cs (1) + He	ΔE_{21} (cm^{-1})	T (K)	Q_{21} $(10^{-16}\ \mathrm{cm}^2)$	Reference
Intra-multiplet mixing					
1	Cs $(6\mathrm{P}_{3/2}) \rightarrow$ Cs $(6\mathrm{P}_{1/2})$	554	311	$(3.9 \pm 0.4) \times 10^{-4}$	[55]
				$(2.7 \pm 0.4) \times 10^{-4}$	[56]
2	Cs $(7\mathrm{P}_{3/2}) \rightarrow$ Cs $(7\mathrm{P}_{1/2})$	181	405	15 ± 3	[58]
			630	15.6 ± 3	[58]
			450	11 ± 2	[59]
			615	11 ± 2	[59]
3	Cs $(8\mathrm{P}_{3/2}) \rightarrow$ Cs $(8\mathrm{P}_{1/2})$	83	420	$\{22.5 \pm 7\}$	[44]
			620	$\{20.6 \pm 6\}$	[44]
4	Cs $(8\mathrm{D}_{5/2}) \rightarrow$ Cs $(8\mathrm{D}_{3/2})$	11.7	360	$\{552 \pm 83\}$	[60]
5	Cs $(9\mathrm{D}_{5/2}) \rightarrow$ Cs $(9\mathrm{D}_{3/2})$	7.2	360	$\{515 \pm 77\}$	[60]
6	Cs $(10\mathrm{D}_{5/2}) \rightarrow$ Cs$(10\mathrm{D}_{3/2})$	4.7	353	$\{503 \pm 100\}$	[61]
7	Cs $(11\mathrm{D}_{5/2}) \rightarrow$ Cs $(11\mathrm{D}_{3/2})$	3.25	353	$\{330 \pm 66\}$	[61]
8	Cs $(12\mathrm{D}_{5/2}) \rightarrow$ Cs $(12\mathrm{D}_{3/2})$	2.3	353	$\{208 \pm 54\}$	[61]
9	Cs $(13\mathrm{D}_{5/2}) \rightarrow$ Cs $(13\mathrm{D}_{5/2})$	1.7	353	$\{175 \pm 54\}$	[61]
10	Cs $(14\mathrm{D}_{5/2}) \rightarrow$ Cs $(14\mathrm{D}_{3/2})$	1.3	353	$\{107 \pm 33\}$	[61]
Intermultiplet mixing					
1	Cs $(7\mathrm{D}_{3/2}) \rightarrow$ Cs $(8\mathrm{P}_{1/2})$	339	420	$\{2.2 \pm 0.7\}$	[44]
2	Cs $(7\mathrm{D}_{5/2}) \rightarrow$ Cs $(8\mathrm{P}_{1/2})$	360	420	$\{1.6 \pm 0.5\}$	[44]
3	Cs $(6\mathrm{D}_{3/2}) \rightarrow$ Cs $(7\mathrm{P}_{3/2})$	642	450	$\{2.1 \pm 0.6\}$	[59]
			615	$\{3.6 \pm 1.0\}$	[59]
4	Cs $(6\mathrm{D}_{3/2}) \rightarrow$ Cs $(7\mathrm{P}_{1/2})$	823	450	$\{1.7 \pm 0.5\}$	[59]
			615	$\{2.7 \pm 0.7\}$	[59]

Legend as for Table 4.

4.7. Temperature dependence of the CEET cross-sections

There are very different forms of temperature dependence for the various thermal CEET cross-sections, as can be concluded from the previous considerations. Unfortunately, systematic, quasi-continuous measurements of this effect, as performed in [56,58], are very rare. Most frequently, the measurements are related to a relatively narrow temperature range, for which the relevant signals in a particular experiment can be measured. Nevertheless, from the data set presented in this paper, an interesting relationship between the magnitude of the exothermic cross-sections and their dependence on temperature can be established. There is a continuous change in dependence from approximately $Q \sim T^2$ to $Q \sim T^{-0.5}$ from the lowest to the highest cross-section in Fig. 10. Here, various

collision partners and various types of CEET processes with different energy defects are included. There are no data in the cross-section databases available that violate the regularity shown in Fig. 10. This means that neither the energy defect nor the type of interaction, but only the absolute magnitude of the thermal cross-sections is crucial for the thermal cross-section temperature behavior. It should be pointed out that cross-sections of the order of 10^{-15} cm^2 are temperature-independent [zero slope of $Q(T)$ in Fig. 10]. This cross-section value is of the same order of magnitude as the geometrical cross-section for the collisions of the atoms involved that are both in their ground states.

It is outside the scope of this paper to propose a possible explanation for the empirical findings. It should be emphasized that numerous models exist that yield good agreement with the experi-
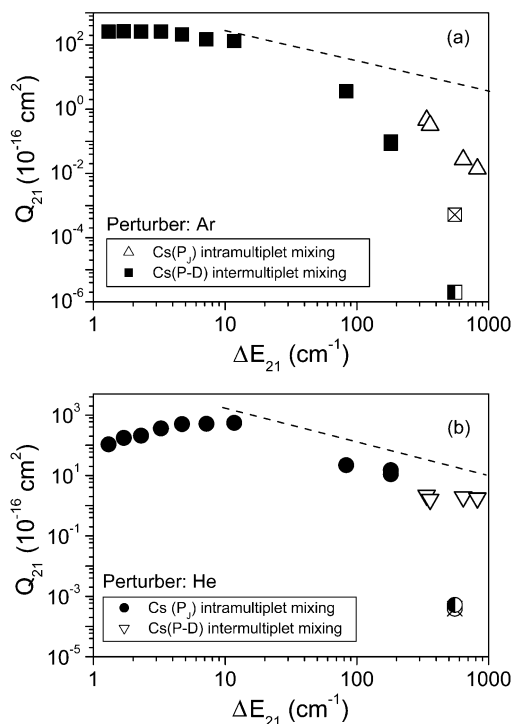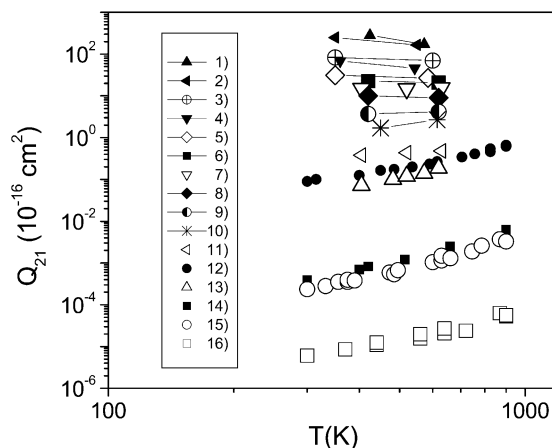
Fig. 10. The temperature dependence of the various exothermic CEET processes in cesium, showing the change of the slope of the $Q(T)$ curve depending on the magnitude of the exothermic cross-section, which spans over eight orders of magnitude. A continuous transformation from a $Q \sim T^2$ to a $Q \sim T^{-0.5}$ dependence can be observed. Various collision partners and various types of CEET processes with different energy defects are included in the figure. (1) Na $(3P_{3/2})$ + Na $(3S) \to$ Na $(3P_{1/2})$ + Na $(3S)$ [22,34]; (2) K $(4P_{3/2})$ + K $(4S) \to$ K $(4P_{1/2})$ + K $(4S)$ [22]; (3) Cs $(6P_{3/2})$ + C$(6P_{3/2}) \to$ Cs $(6D)$ + Cs $(6S)$ [53,54]; (4) Rb $(5P_{3/2})$ + Rb $(5S) \to$ Rb $(5P_{1/2})$ + Rb $(5S)$ [22]; (5) Cs $(6P_{3/2})$ + Cs $(6S) \to$ Cs $(6P_{1/2})$ + Cs$(6S)$ [35,36]; (6) Cs $(8P_{3/2})$ + He $\to$ Cs $(8P_{1/2})$ + He [44]; (7) Cs $(7P_{3/2})$ + He $\to$ Cs $(7P_{1/2})$ + He [58]; (8) Cs $(8P_{3/2})$ + Xe $\to$ Cs $(8P_{1/2})$ + Xe [44]; (9) Cs $(8P_{3/2})$ + Ar $\to$ Cs $(8P_{1/2})$ + Ar [44]; (10) Cs $(6D_{3/2})$ + He $\to$ Cs $(7P_{1/2})$ + He [59]; (11) Cs $(7P_{3/2})$ + Xe $\to$ Cs $(7P_{1/2})$ + Xe [58]; (12) Rb $(5P_{3/2})$ + He $\to$ Cs $(5P_{1/2})$ + He [56]; (13) Cs $(7P_{3/2})$ + Ar $\to$ Cs $(7P_{1/2})$ + Ar [58]; (14) Rb $(5P_{3/2})$ + Xe $\to$ Cs $(5P_{1/2})$ + Xe [56]; (15) Cs $(6P_{3/2})$ + He $\to$ Cs $(6P_{1/2})$ + He [56]; and (16) Cs $(6P_{3/2})$ + Ne $\to$ Cs $(6P_{1/2})$ + Ne [56].

Fig. 9. (a) The cross-sections for intra-multiplet ($nP_{3/2} \to nP_{1/2}$, $nD_{5/2} \to nD_{3/2}$) and inter-multiplet ($nl \to n'l'$) mixing in cesium induced by collisions with argon, plotted in a double logarithmic scale vs. the reaction energy defect ΔE. The data shown are listed in Table 4. The dashed straight line corresponds to the eye-guiding line 1 in Fig. 7. (b) The cross-sections for intra-multiplet ($nP_{3/2} \to nP_{1/2}$, $nD_{5/2} \to nD_{3/2}$) and inter-multiplet ($nl \to n'l'$) mixing in cesium induced by collisions with helium, plotted in a double logarithmic scale vs. the reaction energy defect ΔE. The data displayed are listed in Table 5. The dashed straight line corresponds to the eye-guiding line 1 in Fig. 7.

mental cross-sections, as well as the temperature behavior of the cross-sections for special CEET processes. For example, the theoretical value of the exothermic cross-section (31×10^{-16} cm^2 at 311 K) and its temperature dependence ($\sim T^{-0.6}$) for the case of Cs $(6P_J)$ fine-structure mixing by cesium was found to be in very good agreement with experimental results [36]. On the other hand, as mentioned in the previous section, in [23] a quite different theoretical model yielded a very good description for the strong temperature dependence ($\sim T^2$) of the extremely small cross-

sections for the fine-structure mixing of the alkali first resonance levels due to noble gases. There is no general approach that would connect these different models in a transparent manner. Nevertheless, the systematization given here can be of use for experimentalists in predicting the values if there is a lack of relevant data.

5. Applications related to resonance fluorescence imaging filters

5.1. Spatial resolution of imaging atomic filters

In the following the experimental results published in [8] are discussed as an example of the
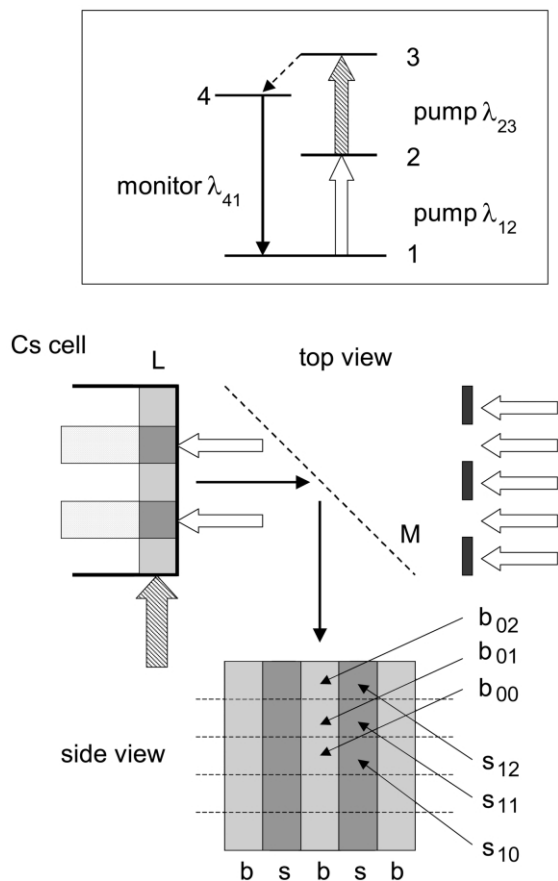
Fig. 11. Schematic diagram of the experiment reported in [3] and discussed in Section 5.1.

application of the radiation trapping approach presented here. In [8], the spatial distortion due to trapping in a Cs atomic-vapor imaging filter has been investigated. For the sake of clarity of this text, a sketch of that experiment is shown in Fig. 11 and the experimental procedure is briefly described. A cell containing Cs metal in vacuum was heated and illuminated by two perpendicular, single-mode diode laser beams. The frequency of the first laser was tuned to a hyperfine component of the Cs D2 resonance line at $\lambda_{12} = 852$ nm. The laser beam was transmitted trough a mask with periodic openings with widths (L) of a few 100 μm. The period was of the same size. In this way, zones of excited (signal zones) and non-excited (background zones) atoms in the vapor were deter-

mined. The second laser beam was transformed into a 12-mm-long sheet with width $L = 0.5$ mm. The second laser was used to pump the transition at $\lambda_{23} = 917$ nm. The spatial distribution of the fluorescence intensity at $\lambda_{41} = 455$ nm was measured while changing the cesium bath temperature in the range between 293 and 318 K. The situation is similar to that described in Section 3.3. Considering the number densities $\bar{N}_2(s)$ and $\bar{N}_2(b)$ in cubic volume elements of size L in the signal and background zones, respectively, we can, according to Eqs. (3.22) and (3.23), state that $\bar{N}_2(s)/\bar{N}_2(b) \propto 1/J_{\text{cub}}$. Since the intensity S of the fluorescence monitored in the signal zone is proportional to $\bar{N}_2(s)$ and the intensity B in the background zone is proportional to $\bar{N}_2(b)$, the S/B ratio can be written as follows [see Eq. (3.18)]:

$$\frac{S}{B} \propto \frac{1}{J_{\text{cub}}} \propto \frac{1}{L\bar{N}_1 P(0)} \qquad (5.1)$$

Obviously, the signal/background ratio depends on L and, for fixed L, exhibits a hyperbolic dependence on the number density in the lowest state ($\bar{N}_1 \approx N_{\text{Cs}}$). This is in agreement with the experimental findings reported in [8]. Note that, according to Eq. (5.1), we can improve the signal/background ratio at fixed L and $\bar{N}_1$ by increasing the line broadening [see Eq. (2.3)].

It is apparent that a volume of slab form is the most appropriate geometry for an atomic imaging filter, but it should be noted that the working scheme in Fig. 11, i.e. in Ref. [8], is not the best choice for simulation of slab geometry. Namely, the pumping of resonance level 2 in the experiment sketched in Fig. 11 is not limited to the regions defined by the beam size of the second pump laser, but spreads over the whole cell volume. Since diffusion of the resonance radiation depends on the size of the volume excited in the first step, the number density of the resonantly excited atoms in the thin slice just behind the entrance cell window illuminated by the second laser at λ_{23} is strongly influenced by the rest of the excited volume beyond that slice. Consequently, the monitored fluorescence emerging from the signal and background zones, i.e. signal/background ratio,

depends on the size of the excited volume extending beyond the thin slice observed. With the cylindrical cell used, a much better signal/background ratio would be obtained by simple interchange of the directions of lasers λ_{12} and λ_{23}. In such a case, only atoms in the thin vapor layer behind the cell window would be originally excited to the resonance state, and the situation would be closer to the imaging filter with slab geometry.

In order to obtain further insight into the processes that influence the spatial resolution of imaging filters, we apply here the approach presented in Section 3 to a volume of slab form. We consider the volume to be an infinite slab with thickness L, which is divided in cubic elements of volume L^3, and is illuminated in the same way as illustrated in Fig. 11. According to Eqs. (3.6) and (3.7) and the procedure in Section 3.3, we can establish the following rate equation for the average density $\bar{N}_2(b_{00})$ in the central cubic element b_{00}:

$$
\begin{aligned}
A_{21}^{\text{eff}}\big[\bar{N}_2(b_{00}) \\
- 2L^3\Phi_{01}\bar{N}_2(b_{01}) - 2L^3\Phi_{02}\bar{N}_2(b_{02}) - \ldots \\
- 4L^3\Phi_{10}\bar{N}_2(s_{10}) - 4L^3\Phi_{11}\bar{N}_2(s_{11}) - \ldots\big] \\
= 0
\end{aligned}
\tag{5.2}
$$

Here, similarly to Eq. (3.25), the coefficients Φ_{mn} are given by:

$$
\Phi_{mn} = \frac{a_1^{\text{P}}k_0^{\text{P}}L}{4\pi(m^2+n^2)}\exp\left[-\sqrt{m^2+n^2}\,k_0^{\text{P}}/b^{\text{P}}\right]
\tag{5.3}
$$

If we assume isotropic pumping and take an infinite slab, it follows that $\bar{N}_2(b_{00}) = \bar{N}_2(b_{0n}) \equiv \bar{N}_2(b)$ and $\bar{N}_2(s_{10}) = \bar{N}_2(s_{1m}) \equiv \bar{N}_2(s)$. In this case, Eqs. (5.2) and (5.3) yield the following expression for the signal/background ratio:

$$
\begin{aligned}
\frac{S}{B} &= \frac{\bar{N}_2(s)}{\bar{N}_2(b)} \\
&= \frac{1 - \dfrac{a_1^{\text{P}}k_0^{\text{P}}L}{2\pi}\displaystyle\sum_{m=1}^{\infty}\frac{1}{m^2}\exp\left[-mk_0^{\text{P}}L/b^{\text{P}}\right]}{\dfrac{a_1^{\text{P}}k_0^{\text{P}}L}{\pi}\displaystyle\sum_{n=0}^{\infty}\frac{1}{1+n^2}\exp\left[-\sqrt{1+n^2}\,k_0^{\text{P}}L/b^{\text{P}}\right]}
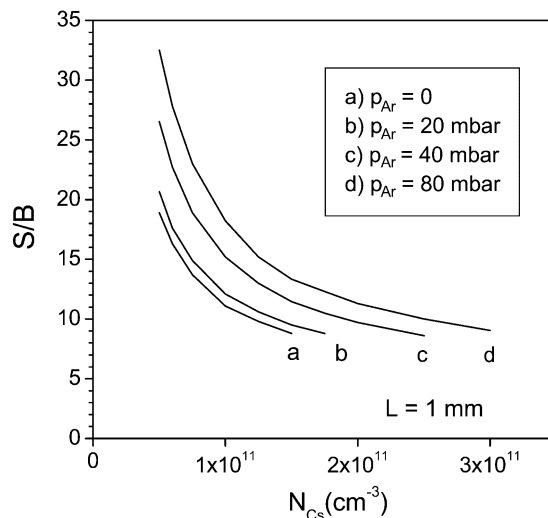\end{aligned}
\tag{5.4}
$$

Fig. 12. Calculated signal/background ratio S/B as a function of cesium number density for various argon pressures. The calculations refer to the excitation scheme applied in Ref. [8] and to the case of a practically infinite, 1-mm-thick slab.

Under the assumption that the slab contains pure cesium vapor, the cesium resonance lines are essentially Doppler-broadened in the temperature range considered of 293–318 K (see Appendix D). The mean Δ_{G} for the Cs D2 line is 385 MHz, but the effective Δ_{G}' for two unresolved groups of hyperfine components (see Appendix B) is approximately $1.5 \times \Delta_{\text{G}}$. Taking this into account, we obtain the peak absorption coefficient $k_0^{\text{P}} = k_0^{\text{D}}$ $(\text{cm}^{-1}) = 3.02 \times 10^{-11} \times N_{\text{Cs}}$ $(\text{cm}^{-3})L$ (cm). In the present simulation the value $L = 1$ mm was taken. The results calculated for S/B are plotted in Fig. 12 as a function of the cesium number density for the case of pure cesium vapor and in the presence of argon at $p_{\text{Ar}} = 20$, 40 or 80 mbar. Here, the value for the collision broadening parameter $\gamma_{\text{Ar}}^{\nu} = 2.9 \times 10^{-10}$ s^{-1} cm^3 at the actual temperature was used, which was obtained from the data given in Appendix D. The calculations were limited according to Eq. (3.18) and carried out using Eqs. (2.3) and (2.4) for evaluation of peak values for the absorption coefficient with a Voigt line shape.

As can be observed from Fig. 12, the presence of the foreign gas increases the spatial resolution. Certainly, better resolution can be gained simply
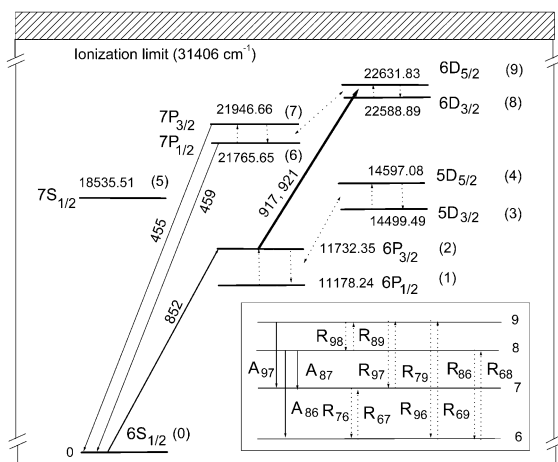
Fig. 13. Partial term diagram of cesium showing the excitation scheme and the most probable collision-induced transitions in a Cs + noble gas mixture (*dotted arrows*). For the sake of simplicity, the sets of the inter-multiplet CEET transitions are represented by single dotted lines with arrows at both ends. The numbers attributed to the levels are the energies given in cm^{-1}. The numbers in brackets are labels of the levels. The inset shows radiative (*full arrows*) and collision-induced transitions (*dotted arrows*) between the Cs $6D_J$ and $7P_J$ states.

5.2. Influence of CEET on population distributions

The pumping scheme of the previous section is often applied in experiments dealing with Cs resonance fluorescence imaging filters [6–10]. As pointed out in [4], the near-infrared wavelength to be detected (Cs D2 line) is useful for many applications in which visible and ultraviolet photons are strongly absorbed in the medium examined, for example in biological tissue [9]. In the first step, the weak signal input excites the Cs atoms to the resonance $6P_{3/2}$ state (see Fig. 13). In the second step, using a high-power laser beam at either 917 or 921 nm, the states $6D_{5/2}$ or $6D_{3/2}$, respectively, are excited with maximum saturation. Due to subsequent radiative relaxation, the $6D_J$ states are mainly depopulated by $6D_J \rightarrow 6P_{J'}$ transitions, and with weaker branching by the $6D_J \rightarrow 7P_{J'}$ transitions. The output signals are observed at wavelengths of 455 and 459 nm belonging to the Cs second resonance transition. The signal output yield can be expressed as the ratio of the population densities in the relevant $7P_J$ and $6D_J$ states. In Table 6 the theoretical values for the total radiative relaxation rates $\sum_i A_{ki} = 1/\tau_k$ are given, where τ_k is the lifetime of the state k considered. In addition, the radiative rates for the $6D_J \rightarrow 7P_{J'}$ multiplet are listed in Table 6. As a consequence of the branching ratios, the output signals at 455 and 459 nm are very weak. Nevertheless, this situation can be significantly improved when CEET processes are involved, which is discussed in the following.

by lowering N_{Cs}, but this causes a decrease in the quantum efficiency of the imaging filter. On the other hand, it is important to bear in mind the negative influence of the line broadening on the spectral bandwidth of imaging filters [4]. The approximate approach presented can be used to find compromise conditions for the spatial resolution with respect to the efficiency required, as well as spectral resolution in the particular excitation and de-excitation scheme.

Table 6
The total radiative relaxation rates $1/\tau$, where τ is the lifetime of the particular sublevel of the Cs $6D_J$ or $7P_J$ doublet, and radiative rates A_{ki} for the $6D_J \rightarrow 7P_{J'}$ multiplet

Transition	$k \rightarrow i$	$(1/\tau_k)$ (10^7 s^{-1})	$(1/\tau_i)$ (10^7 s^{-1})	λ_{vac} (μm)	A_{ki} (10^7 s^{-1})
$6D_{5/2} \rightarrow 7P_{3/2}$	$9 \rightarrow 7$	1.66[a]	0.71[a]	12.147	0.0064[b]
$6D_{3/2} \rightarrow 7P_{3/2}$	$8 \rightarrow 7$	1.66[a]		15.570	0.0009[b]
$6D_{3/2} \rightarrow 7P_{1/2}$	$8 \rightarrow 6$		0.71[a]	14.595	0.0074[b]

The indices k and i are related to labeling of levels displayed in Fig. 13.
[a] Results from [62].
[b] The values calculated via oscillator strengths published in [63].

We consider the Cs vapor cell at 320 K, a typical temperature for a Cs resonance fluorescence imaging filter. The corresponding Cs number density is approximately 3×10^{11} cm^{-3} (see Appendix C). The cell is additionally filled with buffer gas (Ar or He) at a given, relatively low pressure (order of magnitude: several mbar). In Fig. 13, the most probable CEET transitions under the experimental conditions selected are indicated by dotted lines.

With all radiative rates included (not displayed in Fig. 13), the system can be described by a set of 10 coupled rate equations for the population densities in the states considered. Bearing in mind the weak $6S_{1/2} \rightarrow 6P_{3/2}$ and the strongly pumped $6P_{3/2} \rightarrow 6D_J$ transitions, the configuration can be reduced and consideration can be focused on the four-level system comprising the states $7P_{1/2}$, $7P_{3/2}$, $6D_{3/2}$ and $6D_{5/2}$ labeled with 6, 7, 8 and 9, respectively. The radiative and collision-induced transitions related to this four-level system are sketched in the inset of Fig. 13. The corresponding rate equations for the population densities N_6, N_7, N_8 and N_9 can be written in matrix form as follows:

$$
\begin{pmatrix}
(-1/\tau_6 + S_{6n}) & R_{76} & A_{86}+R_{86} & R_{96} \\
R_{67} & (-1/\tau_7 + S_{7n}) & A_{87}+R_{87} & A_{97}+R_{97} \\
R_{68} & R_{78} & (-1/\tau_8 + S_{8n}) & R_{98} \\
R_{69} & R_{79} & R_{89} & (-1/\tau_9 + S_{9n})
\end{pmatrix}
$$
$$
\times \begin{pmatrix} N_6 \\ N_7 \\ N_8 \\ N_9 \end{pmatrix} = \begin{pmatrix} 0 \\ 0 \\ -\Pi_{28} \\ -\Pi_{29} \end{pmatrix}
$$

$$(5.5)$$

where $S_{mn} = \sum\limits_{n \neq m} R_{mn}$. The collision rates R_{mn} are the sums of the contributions

$$R_{mn} = \sum_X R_{mn}^X = \sum_X Q_{mn}^X \langle v_{Cs-X} \rangle N_X \qquad (5.6)$$

where X = Cs, Ar or He. Under the experimental conditions assumed here, $\langle v_{Cs-Cs} \rangle N_{Cs}$ is 6.8×10^{15} cm^{-2} s^{-1} and, in spite of the large cross-sections for $7P_J$ and $6D_J$ intra-multiplet mixing by cesium

(see numbers 2 and 5 in Table 3a), the corresponding collision rates are small ($\sim 10^2$ s^{-1}) compared with the weak radiative rates for the Cs $6D_J \rightarrow 7P_J$ transitions. The cross-section data for the Cs $6D \leftrightarrow 7P$ inter-multiplet mixing by cesium have not been measured yet. However, they can be estimated to be in the range between 20×10^{-16} and 200×10^{-16} cm^2 (see Fig. 7), which means that in the present case all CEET contributions by cesium can be neglected.

On the other hand, we can produce large collision mixing rates by noble gas pressure variation and by the addition of other gases. An interesting enhancement of the $N(7P)/N(6D)$ ratio appears when helium is used as a buffer gas. This can be observed if we adjust the collision rates R_{mn} to fall in the range $A < R_{mn} \ll 1/\tau_m$. Then, if, for example, state 8 is pumped ($\Pi_{28} \neq 0$, $\Pi_{29} = 0$), the system in Eq. (5.5) yields the following expressions for the population ratios:

$$\frac{N_6}{N_8} \approx \frac{A_{86}+R_{86}}{(1/\tau_6)} \qquad (5.7)$$

$$\frac{N_7}{N_8} \approx \frac{A_{87}+R_{87}}{(1/\tau_7)} \qquad (5.8)$$

At pressure of 1 mbar and $T = 320$ K, the products $\langle v_{Cs-He} \rangle N_{He}$ and $\langle v_{Cs-Ar} \rangle N_{Ar}$ are 2.6×10^{21} and 9.4×10^{21} cm^{-2} s^{-1}, respectively, which in combination with the values predicted for the corresponding cross-sections at the temperature chosen (see Table 7) yields $R_{86}^{He} = 3.1 \times 10^5$ s^{-1}, $R_{87}^{He} = 3.9 \times 10^5$ s^{-1}, $R_{86}^{Ar} = 6.6 \times 10^2$ s^{-1} and $R_{87}^{Ar} = 1.4 \times 10^3$ s^{-1}. The present consideration shows that, as a consequence of the relatively large inter-multiplet mixing cross-sections, helium can significantly enhance the $N(7P)/N(6D)$ ratio in comparison with the case when the 7P states are populated only by radiative transitions. Argon as a buffer gas is more than two orders of magnitude less effective than helium, and comparable results to those obtained with helium would require much higher argon pressures.

To examine the relationships between the population densities of involved $7P_J$ and $6D_J$ substates in a wider pressure region, we have to take account

of the other mixing processes. Unfortunately, the set of cross-sections (see Table 7) is incomplete. Experimental data for the $6D_J$ intra-multiplet mixing, as well as for the $6D_{5/2} \rightarrow 7P_J$ inter-multiplet mixing, by noble gases are not available. To obtain further insight into the effect discussed, we used estimated values (see Table 7) which, for a given collision pair, can be obtained on the basis of the general behavior of the cross-sections as a function of temperature and energy defect presented in Section 4. With these data, numerical solutions to the system in Eq. (5.5) were obtained and the results are shown in Fig. 14. In this model, $\Pi_{28} = 0$ and $\Pi_{29} \neq 0$ were chosen for the pumping of the transition $6P_{3/2} \rightarrow 6D_{5/2}$.

As can be observed in Fig. 14a, the $7P_J$ and $6D_J$ states are completely mixed at helium pressure of approximately 10 mbar, and the sublevel population ratios N_6/N_7 and N_8/N_9 reach equilibrium values of 1.13 and 0.81, respectively, at $T = 320$ K. For argon, complete intra-multiplet mixing occurs at pressure of several 100 mbar. The remarkable difference between helium and argon can be recognized when viewing the inter-multiplet population density ratios shown in Fig. 14b,c for lower and higher pressures, respectively. Due to
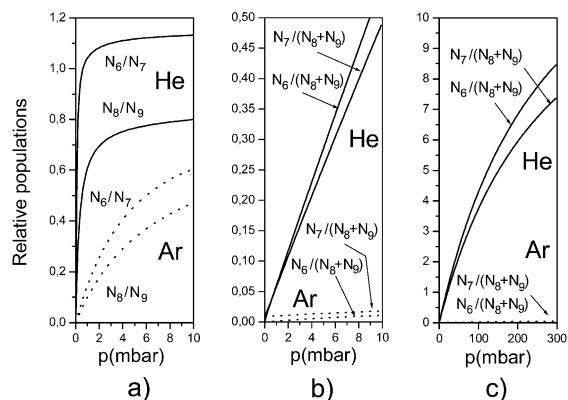

Fig. 14. (a) The calculated relative populations of the Cs $7P_J$ (N_6/N_7) and the Cs $6D_J$ (N_8/N_9) sub-states as a function of buffer gas pressure in the case when the $6D_{5/2}$ state is optically excited. The calculated ratios $N_i/(N_8 + N_9)$ as a function of buffer gas pressure up to (b) 10 and (c) 300 mbar.

the strong inter-multiplet mixing rates by He, the relative populations in the 7P and 6D states become much higher than those produced by radiative transitions. In contrast, argon is a very weak collision mixer, since its mixing rates are approximately 300-fold smaller than for helium.

Table 7
The collision cross-sections for the CEET between the Cs $6D_J$ and $7P_J$ levels by argon and helium

Transition	$k \rightarrow i$	ΔE_{ki} (cm^{-1})	X	Q_{ki}^{X} (10^{-16} cm^2)		
				Experimental values at different T	Predicted at $T = 320$ K	Estimated at $T = 320$ K
$6D_{5/2} \rightarrow 6D_{3/2}$	$9 \rightarrow 8$	43	Ar	–		~ 20
			He	–		~ 150
$7P_{3/2} \rightarrow 7P_{1/2}$	$7 \rightarrow 6$	181	Ar	0.072	0.045	
			He	15	15	
$6D_{5/2} \rightarrow 7P_{3/2}$	$9 \rightarrow 7$	685	Ar	–		~ 0.015
			He	–		~ 1.5
$6D_{5/2} \rightarrow 7P_{1/2}$	$9 \rightarrow 6$	866	Ar	–		~ 0.007
			He	–		~ 1.2
$6D_{3/2} \rightarrow 7P_{3/2}$	$8 \rightarrow 7$	642	Ar	0.029	0.015	
			He	2.1	1.5	
$6D_{3/2} \rightarrow 7P_{1/2}$	$8 \rightarrow 6$	823	Ar	0.014	0.007	
			He	1.7	1.2	

Experimental values at different temperatures that are listed here have been taken from Tables 4 and 5. The values at 320 K were predicted taking into account Section 4.7 and Fig. 8. The data that have not been measured yet are estimated on the basis of the general dependence of the cross-sections on the energy defect for the particular Cs + X collision pair. The indices k and i are related to labeling of levels displayed in Fig. 13.

The ratios $N_i/(N_8+N_9)=N(7P_J)/N(6D)$ for helium are approximately 0.5 at 10 mbar (Fig. 14b) and approach equilibrium values of the order of 10 beyond 300 mbar (Fig. 14c).

Therefore, it is recommended to add an appropriate amount of helium to the atomic line detector considered. However, experimental proof is required, since the model presented is based on partly interpolated data. In such experiments, undesired side effects in the cesium imaging detector should also be checked for, for example a reduction in spectral resolution due to broadening of the cesium spectral lines by helium. In that case, a compromise between the efficiency and the spectral resolution has to be found.

6. Summary

In this work, the processes of laser excitation, diffusion of resonance radiation and the collision excitation energy transfer were considered. The methods presented enable straightforward qualitative as well as quantitative analysis of the population distributions in neutral thermal gaseous media.

The narrow-band laser excitations of inhomogeneously (Doppler) and homogeneously (Lorentzian) broadened transitions were analyzed and the pumping rates were determined, taking into account the laser beam intensity and the broadening parameters of the line profiles.

The problem of trapping and diffusion of resonance radiation was defined in terms of additional pumping rates appearing in dense excited media. Using the rate equation approach, the Holstein integral equation for the spatially dependent, excited atomic number densities was derived in a straightforward procedure. The steps by which the trapping problem was treated implies plausible ways for quantitative treatments of effective radiative rates and diffusion-like transport of excitation energy. Easy-to-handle formulas for optically quasi-thin conditions were derived.

The elements of the experimental and theoretical treatment of the thermal collisions producing the excitation energy transfer were given. A large body of CEET cross-sections for the Cs+Cs, Cs+Ar and Cs+He systems was collected, listed and analyzed. An empirical dependence of the thermal cross-sections on the energy defect, as well on the temperature, was presented.

The results were used to model the spatial resolution and the quantum efficiency of Cs-based resonance imaging filters.

Acknowledgments

Appendix A: Definitions and units

In the following, the notation, definitions and units of the physical quantities most frequently used in this paper are listed. The indices i and k correspond to the lower and upper states, respectively.

N_i, N_k: number densities (m^{-3})

g_i, g_k: statistical weights

A_{ki}: Einstein coefficient for spontaneous emission, spontaneous emission rate (s^{-1})

Π_{ik}: pumping rate for the $i \rightarrow k$ transition (s^{-1})

$I^\nu(\nu)$: frequency-dependent spectral intensity $(J\ m^{-2}\ Hz^{-1}\ s^{-1})$

c: velocity of light $(m\ s^{-1})$

e: electron charge (C)

m: electron mass (kg)

k: Boltzmann constant $(kg\ K^{-1})$

h: Planck constant $(J\ s)$

ν_{ik}: central frequency of the spectral line

f_{ik}: oscillator strength of the spectral line

$k_{ik}(\nu)=KN_iP(\nu)$: frequency-dependent linear absorption coefficient (m^{-1})

K: $(\pi e^2/mc)f_{ik}$ $(m^2\ Hz)$

$P(\nu)$: normalized $[\int P(\nu)d\nu=1]$ line profile (Hz^{-1})

$k_0^P = KN_iP(0)$: peak value of the absorption coefficient

$P_D(\nu) = (\sqrt{\pi}\Delta\nu_D)^{-1}\exp[-\{(\nu-\nu_{ik})/\Delta\nu\}^2]$: normalized Doppler (Gauss) profile (Hz^{-1})

$\Delta\nu_D = (\nu_{ik}/c)(2kT/M)^{1/2}$: Doppler broadening parameter (Hz)

$\Delta_G = 2\sqrt{\ln 2}\cdot\Delta\nu_D$: full-width at half-maximum of the Gauss (Doppler) profile (Hz)

$P_D(0) = 2\sqrt{\ln 2/\pi}/\Delta_G = 1/(\sqrt{\pi}\Delta\nu_D)$: peak value of the normalized Doppler profile (Hz^{-1})

$P_L(\nu) = (\Gamma_\nu/2\pi)/[(\nu-\nu_{ik})^2 + (\Gamma_\nu/2)^2]$: normalized Lorentzian profile (Hz^{-1})

$\Delta_L = \Gamma_\nu$: full-width at half-maximum of the Lorentzian profile (Hz)

$P_L(0) = 2/(\pi\Delta_L)$: peak value of the normalized Lorentzian profile (Hz^{-1})

Appendix B: Hyperfine structure of the cesium D1 and D2 lines

The total energy of an atomic level can be presented as a sum [64]:

$$E_F = E_J + E_{M1} + E_{E2} = E_J + \frac{h}{2}AK$$

$$+ \frac{3h}{8}B\frac{K(K+1) - \frac{4}{3}I(I+1)J(J+1)}{I(2I-1)J(2J-1)}, \quad I,J \geq 1 \tag{B1}$$

where E_J is the energy of the level in the case of zero interaction of the electrons with the nucleus, E_{M1} is the interaction energy for the system electrons–nuclear dipole moment, E_{E2} is the interaction energy for the system electrons-nuclear quadrupole moment, while J, I and F have their usual meaning. The quantity $K = F(F+1) - I(I+1) - J(J+1)$, and A and B are the hyperfine splitting constants of the atomic energy levels. For the cesium $6S_{1/2}$ and $6P_{3/2}$ states, $A_{1/2} = 292$ MHz, $B_{1/2} = 0$ and $A_{3/2} = 50.3$ MHz, $B_{3/2} = -0.4$ MHz, respectively [64].
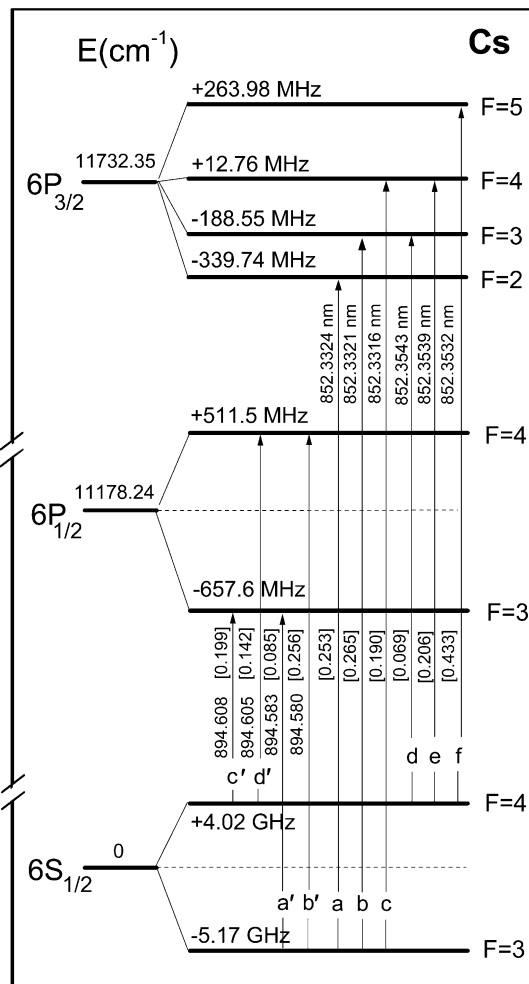

Fig. B1. Hyperfine splitting of the cesium $6S_{1/2}$, $6P_{1/2}$ and $6P_{3/2}$ levels with the transition wavelengths (in nm), oscillator strengths (in square brackets) and level separations.

The hyperfine splitting of the cesium $6S_{1/2}$, $6P_{1/2}$ and $6P_{3/2}$ levels is shown in Fig. B1, while Fig. B2 shows the structure and shape of the Doppler-broadened D1 and D2 lines for $T = 300$ K.

General expressions for the line strength of the hyperfine component connecting F and F' relative to the line strength at the $J \rightarrow J'$ transition can be found in [65] in the form of $3-j$ coefficients. The evaluation yields expressions for the relative line intensities of the transitions $(a'IJ'F') \Rightarrow (aIJF)$
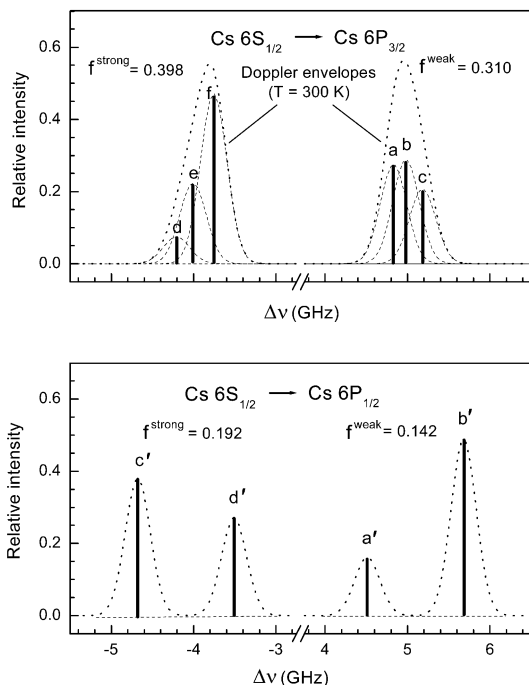
Fig. B2. The shape and the structure of the Doppler-broadened cesium D1 (*bottom*) and D2 (*top*) line at $T = 300$ K. Hyperfine components are represented by dotted lines and labeled with a, b, c, etc. Dashed lines indicate Doppler envelopes for the strong and weak components of the $6S_{1/2} \rightarrow 6P_{3/2}$ and $6S_{1/2} \rightarrow 6P_{1/2}$ transitions.

numbers different from I, J, J', F and F', which have their usual meanings.

The intensity I of the spectral line occurring at the transition $(a'IJ'F') \Rightarrow (aIJF)$ between hyperfine components is:

$$I(F' \rightarrow F) \sim f(F' \rightarrow F) \cdot N(F') \qquad (B2)$$

where $f(F' \rightarrow F)$ is the oscillator strength of the transition and $N(F')$ is the number of atoms in the state $(a'IJ'F')$ given by:

$$N(F') = g(F') \cdot N_0 \qquad (B3)$$

where N_0 is the total number of atoms in the initial state and:

$$g(F') = \frac{n_F}{n_{tot}} = \frac{2F'+1}{\displaystyle\sum_{F'=|J'-I|}^{F'=J'+I}(2F'+1)} \qquad (B4)$$

is the relative statistical weight of the $(a'IJ'F')$ level defined as the ratio of the number of states of the $(a'IJ'F')$ level n_F to the total number of states of the initial level n_{tot}.

The ratios of the relative intensities of the lines at the transitions between hyperfine levels:

$$\frac{I(F' \rightarrow F)}{I(\tilde{F}' \rightarrow \tilde{F})} = \frac{f(F' \rightarrow F)}{f(\tilde{F}' \rightarrow \tilde{F})} \cdot \frac{2F'+1}{2\tilde{F}'+1},$$
$$F', \tilde{F}, \tilde{F}' = F, F \pm 1 \qquad (B5)$$

between hyperfine components of the atomic levels. The expressions are given in Table B1 for two types of $J' \rightarrow J$ transitions, i.e. for $J' = J$ and $J' = J - 1$. Symbols a and a' stand for all other quantum

Table B1
The relative intensities of the transitions $(a'IJ'F') \Rightarrow (aIJF)$ between hyperfine components of atomic levels

$F' \Rightarrow F$	Line intensity I $(F' \rightarrow F)$	
	$J \Rightarrow J$ transitions	$J-1 \Rightarrow J$ transitions
$F-1 \Rightarrow F$	$-A\dfrac{(J+I+2+F)(J+I-F)(J-I+1+F)(J-I-1-F)}{F+1}$	$B\dfrac{(J+F+I+1)(J+F+I)(J+F-I)(J+F-I-1)}{F}$
$F \Rightarrow F$	$A\dfrac{(2F+1)[F(F+1)+J(J+1)-I(I+1)]^2}{F(F+1)}$	$-B\dfrac{(2F+1)(J+F+I+1)(J+F-I)(J-F+I)(J-F-I-1)}{F(F+1)}$
$F+1 \Rightarrow F$	$-A\dfrac{(J+I+1+F)(J+I+1-F)(J-I+F)(J-I-F)}{F}$	$B\dfrac{(J-F+I)(J-F+I-1)(J-F-I-1)(J-F-I-2)}{F+1}$

A and B are the proportionality constants.

yield oscillator strength ratios that allow determination of the oscillator strength for each particular transition if the oscillator strength for the $(a'IJ') \Rightarrow (aIJ)$ transition is known.

For cesium, $I = 7/2$ and the oscillator strengths for $6S_{1/2} \rightarrow 6P_{1/2}$ and $6S_{1/2} \rightarrow 6P_{3/2}$ are 0.341 and 0.708 [62], respectively.

If we consider each hyperfine sublevel of the ground state, then:

$$f_a + f_b + f_c = f_d + f_e + f_f = f_{3/2} = 0.708 \qquad (B6)$$

and

$$f_{a'} + f_{b'} = f_{d'} + f_{e'} = f_{1/2} = 0.341 \qquad (B7)$$

for the D2 and D1 lines, respectively. Using Eqs. (B6) and (B7) and the set of oscillator strengths ratios from Eq. (B5), the oscillator strength for each hyperfine component can be determined. The results are shown in Fig. B1.

If we look at the ground state as a whole, the weak and strong components of the D2 and D1 lines are as follows:

$$f_{weak}^{D2} = g_{F=4}(f_a + f_b + f_c) = 0.310,$$
$$f_{strong}^{D2} = g_{F=3}(f_d + f_e + f_f) = 0.398 \qquad (B8)$$

$$f_{weak}^{D1} = g_{F=4}(f_{a'} + f_{b'}) = 0.142,$$
$$f_{strong}^{D1} = g_{F=3}(f_{c'} + f_{d'}) = 0.192 \qquad (B9)$$

where $g_{F=3} = 7/16$ and $g_{F=4} = 9/16$ denote the relative statistical weights [Eq. (B4)] of the ground-state hyperfine sublevels with $F = 3$ and $F = 4$, respectively.

Appendix C: Cesium vapor pressure curve

According to Nesmeyanov [66] the data for cesium vapor pressure published by Taylor and Langmuir [67] may be considered as the most reliable. Not long ago, their data were confirmed by measurements of the absorption coefficient in the quasi-static wing of the self-broadened cesium resonance lines [29]. The vapor pressure data for liquid cesium given in [67] are as described by the following equation:
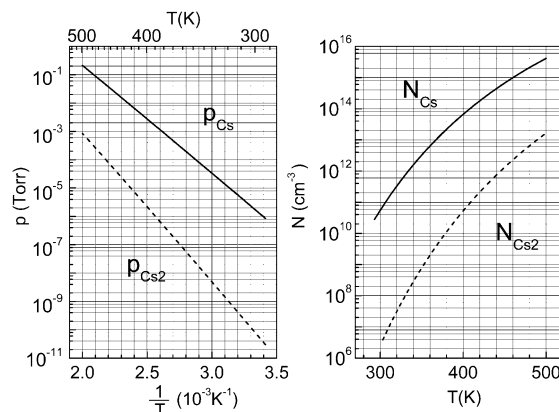

Fig. C1. The Cs and Cs$_2$ vapor pressure curves plotted against $1/T$ (*left*) and the corresponding atom number densities vs. T (*right*). Full and dashed lines correspond to Cs and Cs$_2$ data, respectively. The Cs vapor pressure was calculated according to Eq. (C1), while the Cs$_2$ vapor pressure curve represents the results obtained from Eq. (C4) where the data in [67] for the Cs atom number density N were used.

$$\log p_{Cs} = 11.0531 - \frac{4041}{T} - 1.35 \times \log T \qquad (C1)$$

and are shown in Fig. C1, together with the corresponding atom number density N obtained from $p = NkT$.

The vapor pressure curve given by Nesmeyanov [66] should also be mentioned, with the remark that it differs form the Taylor and Langmuir curve by at most 16% in the temperature range from 293 to 573 K. The Nesmeyanov plot for liquid cesium:

$$\log p_{Cs} = 8.22127 - \frac{4006.048}{T} - 6.0194$$
$$\times 10^{-4} \times T - 0.19623 \times \log T \qquad (C2)$$

was obtained as a weighted statistical average of the data published up to 1963. In the above, as well as in the following relations, the pressure is expressed in Torr.

The vapor pressure curve for cesium dimers can also be found in Nesmeyanov [66], as follows:

$$\log p_{Cs_2} = 18.22054 - \frac{6064.472}{T} + 9.016$$
$$\times 10^{-5} \times T - 3.45395 \times \log T \qquad (C3)$$

Table D1
Line broadening parameters for the first and the second resonance doublet of cesium due to Ar, He and Cs

Transition	λ_{vac} (nm)	γ^ν_{Ar} (s^{-1} cm^3)	γ^ν_{He} (s^{-1} cm^3)	γ^ν_{Cs} (s^{-1} cm^3)
Cs $6S_{1/2} \rightarrow$ Cs $6P_{3/2}$	852.3	$(3.4 \pm 0.5) \times 10^{-10a}$	$(3.6 \pm 0.5) \times 10^{-10a}$	$(6.7 \pm 1) \times 10^{-7b}$
Cs $6S_{1/2} \rightarrow$ Cs $6P_{1/2}$	894.6	$(2.7 \pm 0.7) \times 10^{-10a}$	$(3.1 \pm 0.5) \times 10^{-10a}$	$(5.7 \pm 1) \times 10^{-7b}$
Cs $6S_{1/2} \rightarrow$ Cs $7P_{3/2}$	455.5	$(1.7 \pm 0.4) \times 10^{-9c}$	$(3.1 \pm 1) \times 10^{-9c}$	–
Cs $6S_{1/2} \rightarrow$ Cs $7P_{1/2}$	459.3	$(1.6 \pm 0.2) \times 10^{-9c}$	$(2.6 \pm 0.5) \times 10^{-9c}$	–

[a] Results from [69] at $T = 503$ K.
[b] Results from [70] at $T = 298$ K.
[c] Best values from [71] at $T = 400$ K.

The density of the cesium molecules is related to the atom number density N by a temperature-dependent equilibrium rate $K_{eq}(T)$ through:

$$N_{Cs_2} = \frac{N^2}{K_{eq}(T)} \qquad (C4)$$

where

$$\begin{aligned} K_{eq}(T) = &\ 1.37 \times 10^{22} \times T^{1/2} \\ &\times \exp(-5.22 \times 10^3/T) \\ &\times [1 - \exp(-60.46/T)] \end{aligned} \qquad (C5)$$

as reported in [45], was obtained using cesium molecular ground-state constants given in [68].

The Cs_2 vapor pressure curve and the corresponding dimer number density N_{Cs_2} vs. T are shown in Fig. C1. The data represent the results obtained according to Eq. (C4), where the data reported in [67] for the Cs atom number density were used. In the temperature range between 293 and 500 K, the Cs_2 vapor pressure curve of Nesmeyanov [Eq. (C3)] lies below the curve given by Eq. (C4). The difference amounts to a factor of three at $T = 293$ K and decreases to 30% at $T = 500$ K.

Appendix D: Line broadening parameters for Cs resonance lines

The broadening parameters γ^ν_{Ar}, γ^ν_{He} and γ^ν_{Cs} for collision broadening of the first and second cesium resonance doublet lines by Ar, He and Cs, respectively, reported in [69–71], are summarized in

Table D1. It should be emphasized that, according to theory [16], the γ^ν_{Cs} of self-broadening does not depend on temperature, while the γ due to foreign-gas van der Waals' broadening shows weak temperature dependence ($\sim T^{0.3}$).

Appendix E: Effective radiative rates for Cs D1 and D2

We consider a long, sealed cylindrical cell (radius R) filled with Cs metal and Ar at pressure p_{Ar} established at $T = 300$ K. The cell is heated in the range between 273 and 450 K, which produces Cs number densities approximately in the range between 10^9 and 10^{15} cm^{-3} (see Appendix C). To estimate the effective radiative rates for cesium resonance lines we use the low-opacity approximation presented in Section 3.4 and the Holstein approximation for high opacities [19]. With interpolation of the results obtained, we can estimate the effective radiative rates over the whole range of Cs number densities considered. It is convenient to present the effective radiative rates as a function of the variable $N_{Cs}R$ and the parameter p_{Ar}.

In the present model, the lines are generally of the Voigt type, with the Gaussian width $\Delta_G = 380\sqrt{T/300}$ MHz. The peak value of the normalized Voigt profile $P_V(0)$ is given by Eqs. (2.13) and (2.14). The values for the coefficient a_1^V, depending on the ratio Δ_G/Δ_L, lie between 0.500 and 0.707. The corresponding width of the Lorentzian contribution can be calculated from $\Delta_L = \Gamma^\nu_{nat} + \Gamma^\nu_{coll} = A/2\pi + \gamma^\nu_{Cs}N_{Cs} + \gamma^\nu_{Ar}N_{Ar}$ (see Section 2.2). Using the data for γ^ν_{Cs} and γ^ν_{Ar} given in Appendix D, the Lorentzian widths $\Delta_L^{(1)}$ and $\Delta_L^{(2)}$

for the D1 and D2 lines, respectively, are expressed in Hz and given by:

$$\Delta_{\rm L}^{(1)} = 4.5 \times 10^6 + 5.7 \times 10^{-7} \frac{(N_{\rm Cs}R)}{R} + 8.2$$
$$\times 10^6 p_{\rm Ar} \ ({\rm mbar}) \qquad ({\rm E1})$$

$$\Delta_{\rm L}^{(2)} = 5.1 \times 10^6 + 6.7 \times 10^{-7} \frac{(N_{\rm Cs}R)}{R} + 8.2$$
$$\times 10^6 p_{\rm Ar} \ ({\rm mbar}) \qquad ({\rm E2})$$

where $N_{\rm Cs}R$ and R are given in cm^{-2} and cm, respectively. In the low-opacity case, the escape probability $\eta_{\rm a} = A^{\rm eff}/A$ can be calculated as a function of $N_{\rm Cs}R$ and $p_{\rm Ar}$ using a modified Eq. (3.29), as follows:

$$\eta_{\rm a}(i) = (1 - 1.13 a_1^{\rm V} P_{\rm V}(0) \xi(i) N_{\rm Cs}R)$$
$$\times \left(1 - \frac{1}{4} a_1^{\rm V} P_{\rm V}(0) \xi(i) N_{\rm Cs}R \right.$$
$$\left. \sum_{m=1}^{\infty} \frac{\exp(-2m P_{\rm V}(0) \xi(i) N_{\rm Cs}R)}{m^2} \right) \qquad ({\rm E3})$$

where $\xi(i) = (\pi e^2/mc) \times f(i)$ and $f(i)$ is the total oscillator strength of the resonance line considered, which is a simple sum of the contributions of particular hyperfine components in the optically thin case. Otherwise, the calculations become much more complicated.

In the high-opacity case (see Section 2.4), the Holstein approximation yields results for a pure Gaussian and pure Lorentzian line profile. According to [19], the escape probability for the Gaussian line and a cylindrical geometry is given by $\eta = 1.6(k_0^{\rm D}R)^{-1}(\pi\ln(k_0^{\rm D}R))^{-1/2}$. For high optical depths, we can assume that the line kernels of the D1 and D2 lines are fully absorbed, so that the hyperfine structure can be neglected and the transitions can be considered as single lines. Then, for Doppler broadening, the escape probability as a function of $N_{\rm Cs}R$ is given by:

$$\eta_{\rm b}(i) = \frac{1.6}{\xi_{\rm b}(i) N_{\rm Cs}R \sqrt{\pi\ln(\xi_{\rm b}(i) N_{\rm Cs}R)}} \qquad ({\rm E4})$$
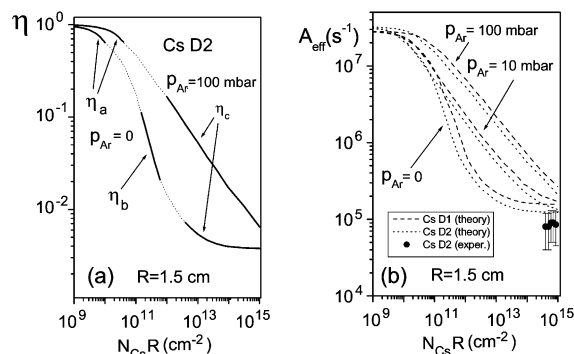

Fig. E1. (a) Construction of the escape probability curves. For detailed explanations see text in Appendix E. (b) Effective radiative rates of the Cs D1 and D2 lines obtained for the cylindrical geometry of the vapor cell. The curves are constructed by combinations of low peak absorption approximation presented in Section 3.4 and the Holstein approximation. For more details see the text in Appendix E.

where $\xi_{\rm b}(i) = 6.08 \times 10^{-11} f(i)$, with $N_{\rm Cs}R$ given in cm^{-2}.

In the case of a pure Lorentzian line form, according to Eq. (2.38) the Holstein escape probability is given as a function of $N_{\rm Cs}R$ and $p_{\rm Ar}$ by the following relation:

$$\eta_{\rm c} = 1.115 \left(\frac{\Delta_{\rm L}^i}{\xi_{\rm c}(i) N_{\rm Cs}R} \right)^{1/2} \qquad ({\rm E5})$$

where $\xi_{\rm c}(i) = \pi \times 1.689 \times 10^{-2} f(i)$, with $N_{\rm Cs}R$ given in cm^{-2}.

The calculated curves $\eta_{\rm a}$, $\eta_{\rm b}$ and $\eta_{\rm c}$ describe the escape probability well only in limited ranges. The results for D2 in pure Cs vapor and at the argon pressure $p_{\rm Ar} = 100$ mbar are given in Fig. E1a. The calculated curves are partially represented by solid and partially by dotted lines. The solid curves are related to ranges in which the particular approximation is estimated to be valid, while the dotted parts describe the regions in which the approximation is invalid. The dashed curves are interpolations between the valid ranges. It should be mentioned that for higher argon pressures, i.e. for pure Lorentzian broadening, this interpolation is much smoother, since the escape probability curve goes from a low-opacity approximation into

the Holstein approximation for a pure Lorentzian profile without inflexion.

As the consequence of the transmission of the trapped radiation in the resonance self-broadened line wings, the escape probabilities [see Eqs. (E1), (E2) and (E4)] saturate in the limit $N_{Cs}R \rightarrow \infty$ at the value $4.33\sqrt{\gamma_{Cs} \ (s^{-1} \ cm^3)/f(i)R} \ (cm)$, which for the D2 line and $R = 1.5$ cm amounts to 3.4×10^{-3}.

The calculations were performed for $p_{Ar} = 0$, 10 and 100 mbar. Using the values for the oscillator strengths given in Appendix B, the effective radiative rates were obtained in the previously explained way, and the results are shown in Fig. E1b. In addition, the experimental results for the effective radiative rate of the D2 line published in [36] are also given. In [36], which deals with the mixing and quenching of the Cs $6P_J$ states by cesium, the experiment was performed in a cell with radius $R = 1.35$ cm and length $L = 13$ cm. The values measured for the effective radiative rate of the Cs D2 line are somewhat lower than the theoretical values presented here. However, taking into account the error bars declared and the uncertainty of the values used for γ_{Cs}, we can conclude that both results are in fair agreement.

It should be stressed that the results for the infinite cylindrical geometry are also approximately valid for the infinite slab if the simple substitution $R \rightarrow L/2$ is made {see Eq. (3.18) and [20]}.

References

[1] J.A. Gelbwachs, 422.7-nm atomic filter with superior solar background rejection, Opt. Lett. 15 (1989) 236–238.

[2] Y.C. Chan, M.D. Tabat, J.A. Gelbwachs, Experimental demonstration of internal wavelength conversion in the magnesium atomic filter, Opt. Lett. 14 (1989) 722–724.

[3] O.I. Matveev, Atomic resonance spectrometers and filters, Zh. Prikl. Spektrosk. (USSR) 46 (1987) 359–375.

[4] O.I. Matveev, B.W. Smith, J.D. Winefordner, Resonance ionization imaging detectors: basic characteristics and potential applications, Appl. Opt. 36 (1997) 8833–8843.

[5] O.I. Matveev, B.W. Smith, J.D. Winefordner, Narrow-band resonance-ionization and fluorescence imaging in a mercury-vapor cell, Opt. Lett. 15 (1998) 304–306.

[6] N.C. Pixley, T.L. Correll, D. Pappas, B.W. Smith, J.D. Winefordner, Sub-Doppler spectral resolution and improved sensitivity in a cesium resonance fluorescence

[7] imaging monochromator, Appl. Spectrosc. 56 (2002) 677–681.

[7] D. Pappas, T.L. Correll, N.C. Pixley, B.W. Smith, J.D. Winefordner, Detection of Mie scattering using a resonance fluorescence monochromator, Appl. Spectrosc. 56 (2002) 1237–1240.

[8] D. Papas, N.C. Pixley, B.W. Smith, J.D. Winefordner, Diffusion of resonance radiation in atomic vapor imaging, Spectrochim. Acta Part B 56 (2001) 1761–1767.

[9] D. Papas, N.C. Pixley, O.I. Matveev, B.W. Smith, J.D. Winefordner, A cesium resonance fluorescence imaging monochromator, Opt. Commun. 191 (2001) 263–269.

[10] D. Papas, N.C. Pixley, B.W. Smith, J.D. Winefordner, Fluorescence monitoring of laser induced population changes of 6P and 6D levels in cesium vapor, Spectrochim. Acta Part B 55 (2000) 1503–1509.

[11] W. Happer, Optical pumping, Rev. Mod. Phys. 44 (1972) 169–249.

[12] W. Demtröder, Laser Spectroscopy, Springer Verlag, Berlin, Heidelberg, New York, 1995.

[13] A.C.G. Mitchell, M.W. Zemansky, Resonance Radiation and Excited Atoms, University Press, Cambridge, 1971.

[14] D.W. Posener, The shape of spectral lines: tables of the Voigt profile, Aust. J. Phys 12 (1959) 184–196.

[15] E.E. Whiting, An empirical approximation to the Voigt profile, J. Quant. Spectrosc. Radiat. Transfer 8 (1968) 1379–1384.

[16] W.E. Baylis, Collisional depolarization in the excited state, in: W. Hanle, H. Kleinpoppen (Eds.), Progress in Atomic Spectroscopy, Part B, Plenum Press, New York and London, 1978, pp. 1227–1297.

[17] A.F. Mölisch, B.P. Oehry, Radiation Trapping in Atomic Vapours, Clarendon Press, Oxford, 1998.

[18] T. Holstein, Imprisonment of resonance radiation in gases, Phys. Rev. 72 (1947) 1212–1233.

[19] T. Holstein, Imprisonment of resonance radiation in gases II, Phys. Rev. 83 (1951) 1159–1168.

[20] A. Gallagher, Line shapes and radiation transfer, in: G.W.F. Drake (Ed.), Atomic, Molecular & Optical Physics Handbook, AIP Press, Woodbury, NY, 1996, pp. 220–232.

[21] H.A. Post, Radiative transport at the 184.9-nm Hg resonance line. I. Experiment and theory, Phys. Rev. A 33 (1986) 2003–2016.

[22] L. Krause, Sensitized fluorescence and quenching, in: J.W. McGowan (Ed.), The Excited State in Chemical Physics, Wiley, New York, 1975, pp. 267–316.

[23] E.E. Nikitin, Theory of non-adiabatic collision processes including excited alkali atoms, in: J.W. McGowan (Ed.), The Excited State in Chemical Physics, Wiley, New York, 1975, pp. 317–377.

[24] A. Thorne, U. Litzén, S. Johanson, Spectrophysics—Principles and Applications, Springer Verlag, Berlin, New York, Tokyo, 1999.

[25] K. Niemax, G. Pichler, New aspects in the self-broadening of alkali resonance lines, J. Phys. B: At. Mol. Phys. 8 (1975) 179–184.

[26] K. Niemax, M. Movre, G. Pichler, Near-wing asymmetries of the self-broadened first Rb and Cs resonance lines, J. Phys. B: At. Mol. Phys. 12 (1979) 3503–3509.

[27] M. Movre, G. Pichler, Resonance interaction and self-broadening of alkali resonance lines II. Quasi-static wing profiles, J. Phys. B: At. Mol. Phys. 13 (1980) 697–707.

[28] M. Krauss, W.J. Stevens, Effective core potentials and accurate energy curves for Cs_2 and other alkali diatomics, J. Chem. Phys. 93 (1990) 4236–4242.

[29] V. Horvatic, M. Movre, R. Beuc, C. Vadla, The non-Lorentzian wings of alkali resonance lines: the determination of the atom number density in pure and mixed alkali vapours, J. Phys. B: At. Mol. Phys. 26 (1993) 3679–3692.

[30] S. Geltman, Theory of energy-transfer collisions of excited sodium atoms: $3P+3P\rightarrow 3S+5S$ or 4D, Phys. Rev. A 40 (1989) 2301–2308.

[31] E.E. Nikitin, S.Ya Umanskii, Theory of Slow Atomic Collisions, Springer Verlag, Berlin, Heidelberg, New York, Tokyo, 1984.

[32] E.E. Nikitin, Adiabatic and diabatic collision processes at low energies, in: G.W.F. Drake (Ed.), Atomic, Molecular & Optical Physics Handbook, AIP Press, Woodbury, NY, 1996, pp. 561–570.

[33] L.D. Landau, E.M. Lifshitz, Quantum Mechanics, Pergamon Press, Oxford, 1965.

[34] J. Huennekens, A. Gallagher, Self-broadening of the sodium resonance lines and excitation transfer between the $3P_{1/2}$ and $3P_{3/2}$ levels, Phys. Rev. A 27 (1983) 1851–1864.

[35] M. Czajkowski, L. Krause, Sensitized fluorescence in vapors of alkali metals III. Energy transfer in cesium–cesium collisions, Can. J. Phys. 43 (1965) 1259–1268.

[36] M. Movre, V. Horvatic, C. Vadla, Caesium 6P fine-structure mixing and quenching induced by collisions with ground-state cesium atoms and molecules, J. Phys B: At. Mol. Opt. Phys. 32 (1999) 4647–4666.

[37] P.S. Julienne, J. Vigué, Cold collisions of ground- and excited-state alkali–metal dimers, Phys. Rev. A 44 (1991) 4464–4485.

[38] C. Vadla, D. Veza, M. Movre, K. Niemax, Fine-structure excitation transfer between the lithium D-lines by collisions with cesium atoms, Z. Phys. D 22 (1992) 591–595.

[39] C. Vadla, M. Movre, V. Horvatic, Sodium 3P fine-structure excitation transfer induced by collisions with rubidium and caesium atoms, J. Phys. B: At. Mol. Opt. Phys. 27 (1994) 4611–4622.

[40] S. Knezovic, C. Vadla, M. Movre, Fine-structure excitation transfer between the potassium 4^2P states induced by collisions with caesium atoms, Z. Phys. D 22 (1992) 449–450.

[41] C. Vadla, S. Knezovic, M. Movre, Rubidium 5^2P fine-structure transitions induced by collisions with potassium and caesium atoms, J. Phys. B: At. Mol. Opt. Phys. 25 (1992) 1337–1345.

[42] C. Gabanini, S. Gozzini, G. Squadrito, M. Allegrini, L. Moi, Energy pooling collisions for K (4P)+Rb (5P) and Na (3P)+Rb (5P) heteronuclear systems, Phys. Rev. A 39 (1989) 6148–6153.

[43] A. Ekers, M. Glodz, V. Grushevsky, J. Kalvins, J. Szonert, Energy transfer between the ^2S and ^2D states in alkalis: experiments and theory, Can. J. Phys. 79 (2001) 1039–1053.

[44] M. Pimbert, Transfert d'excitation électronique, par collision atomique, entre niveaux élevés d'un atome de césium, J. Phys. 33 (1972) 331–343.

[45] A. Sasso, W. Demtröder, T. Colbert, C. Wang, E. Erlacher, J. Huennekens, Radiative lifetimes, collisional mixing, and quenching of the cesium $5D_J$ levels, Phys. Rev. A 45 (1992) 1670–1683.

[46] M. Movre, C. Vadla, V. Horvatic, Mixing and quenching of the Cs $5D_J$ states induced by collisions with caesium ground-state atoms, J. Phys. B: At. Mol. Opt. Phys. 33 (2000) 3001–3012.

[47] A.C. Tam, T. Yabuzaki, S.M. Curry, M. Hou, W. Happer, Inelastic cross-sections in Cs (n^2D_J)+Cs $(6^2S_{1/2})$ collisions, Phys. Rev. A 17 (1978) 1862–1868.

[48] P.W. Pace, J.B. Atkinson, Transfer of electronic excitation between $7^2P_{1/2}$ and $7^2P_{3/2}$ states of cesium induced by collisions with cesium atoms, Can. J. Phys. 52 (1974) 1641–1647.

[49] L. Sirko, K. Rosinski, Fine-structure mixing in Cs atoms excited to intermediate $nD_{5/2}$ states colliding with ground-state Cs atoms, J. Phys. B: At. Mol. Opt. Phys. 18 (1985) L221–L227.

[50] C. Gabbanini, A. Lucchesini, S. Gozzini, Self-quenching mechanism in caesium Rydberg states, J. Phys. B: At. Mol. Opt. Phys. 25 (1992) 3145–3154.

[51] J. Huennekens, A. Sasso, personal communication, 1998.

[52] C. Vadla, K. Niemax, J. Brust, Energy pooling in cesium vapor, Z. Phys. D 37 (1996) 241–247.

[53] C. Vadla, Energy pooling in caesium vapour: Cs^* $(6P_J)+Cs^*$ $(6P_{J'})\rightarrow Cs$ (6S)+Cs^{**} (6D), Eur. Phys. J. D 1 (1998) 259–264.

[54] Z.J. Jabbour, R.K. Namiotka, J. Huennekens, M. Allegrini, S. Milosevic, F. de Tomasi, Energy-pooling collisions in cesium: $6P_J+6P_J$ to $6S+(nl=7P,6D,8S,4F)$, Phys. Rev. A 54 (1996) 1372–1384.

[55] M. Czajkowski, D.A. McGillis, L. Krause, Sensitized fluorescence in vapors of alkali metals V. Energy transfer in collisions between cesium and inert gas atoms, Can. J. Phys. 44 (1966) 91–103.

[56] A. Gallagher, Rubidium and cesium excitation transfer in nearly adiabatic collisions with inert gases, Phys. Rev. 172 (1968) 88–96.

[57] F.S.C. Bruce Pitre, A.G.A. Rae, L. Krause, Sensitized fluorescence in vapors of alkali metals VI. Energy transfer in collisions between rubidium and inert gas atoms, Can. J. Phys. 44 (1966) 731–740.

[58] I.N. Siara, H.S. Kwong, L. Krause, Sensitized fluorescence in vapors of alkali atoms XIV. Temperature

dependence of cross-sections for $7^2P_{1/2}$–$7^2P_{3/2}$ mixing in cesium induced in collisions with noble gas atoms, Can. J. Phys. 52 (1974) 945–949.

[59] J. Cuvellier, P.R. Fournier, F. Gounand, J. Pascale, J. Berlande, Inelastic collisions involving excited cesium atoms at thermal energies, Phys. Rev. A 11 (1975) 846–856.

[60] I. Jackowska, M. Lukaszewski, Cross-sections for J mixing in 8D and 9D states of caesium in collisions with noble-gas atoms, J. Phys. B: At. Mol. Opt. Phys 23 (1990) 2097–2104.

[61] M. Lukaszewski, I. Jackowska, J mixing in nD ($n=$ 10–14) states of caesium induced in collisions with noble-gas atoms, J. Phys. B: At. Mol. Opt. Phys. 24 (1991) 2047–2057.

[62] W. Hansen, The application of polarisation-influenced Thomas–Fermi ion models to alkali-atom transitions, J. Phys. B: At. Mol. Opt. Phys. 17 (1984) 4833–4850.

[63] P.M. Stone, L. Agnew, Plasma-broadened cesium lines, Phys. Rev. 127 (1962) 1157–1162.

[64] A.A. Radzig, B.M. Smirnov, Reference Data on Atoms, Molecules and Ions, Springer-Verlag, Berlin, Heidelberg, New York, Tokyo, 1985, pp. 97–105.

[65] G.T. Emery, Hyperfine structure, in: G.W.F. Drake (Ed.), Atomic, Molecular & Optical Physics Handbook, AIP Press, Woodbury, NY, 1996, pp. 198–205.

[66] A.N. Nesmeyanov, Vapor Pressure of the Chemical Elements, Elsevier, Amsterdam, London, New York, 1963.

[67] J.B. Taylor, I. Langmuir, Vapor pressure of caesium by the positive ion method, Phys. Rev. 51 (1937) 753–760.

[68] H. Weickenmeier, U. Diemer, M. Wahl, M. Raab, W. Demtröder, W. Müller, Accurate ground-state potential of Cs_2 up to the dissociation limit, J. Chem. Phys. 82 (1985) 5354–5363.

[69] F. Siegling, K. Niemax, Low-pressure noble gas broadening of the Cs resonance lines, Z. Naturforsch. 39a (1984) 447–454.

[70] Z.J. Jabbour, J. Sagle, R.K. Namiotka, J. Huennekens, Measurement of the self-broadening rate coefficients of the cesium resonance lines, J. Quant. Spectrosc. Radiat. Transfer 54 (1995) 767–778.

[71] E. Lewis, Collisional relaxation of atomic excited states, line broadening and interatomic interactions, Phys. Rep. 58 (1) (1980) 1–71.